Flow–plant interactions at leaf, stem and shoot scales: drag, turbulence, and biomechanics

Author(s):
Albayrak, Ismail (iD); Nikora, Vladimir; Miler, Oliver; O'Hare, Matthew T.

Aquatic Sciences

Flow–plant interactions at leaf, stem and shoot scales: drag, turbulence, and biomechanics

Ismail Albayrak · Vladimir Nikora ·
Oliver Miler · Matthew T. O'Hare

Abstract Flow–plant interactions are experimentally investigated at leaf, stem, and shoot scales in an open-channel flume at a range of Reynolds numbers. The experiments included measurements of instantaneous drag forces acting on leaves, stems, and shoots of the common freshwater plant species *Glyceria fluitans*, complemented with velocity measurements, high-resolution video recordings, and biomechanical tests of leaf and stem properties. The analyses of bulk statistics, power spectral densities, transfer functions, and cross-correlations of measured velocities and drag forces revealed that flow characteristics, drag force, and plant biomechanical and morphological properties are strongly interconnected and scale-dependent. The plant element–flow interactions can be subdivided into two classes: (I) passive interactions when the drag variability is due to the time variability of the wetted and frontal areas and squared approach velocity (due to the large-scale turbulence); and (II) active inter-actions representing a range of element-specific instabilities that depend on the element flexural rigidity and morphology. Implications of experimental findings for plant biophysics and ecology are briefly discussed.

List of symbols

ADV	Acoustic Doppler velocimeter
A	Reference area
A_f	Frontal projection area of plant
A_i	Characteristic plant diameter × lateral projection plant height
A_w	Total wetted area
α	Vogel number
B	Mean leaf width or mean stem diameter
C_d	Drag coefficient
C_{d-FPL}	Drag coefficient of laminar flat plate flow
C_{d-FPT}	Drag coefficient of turbulent flat plate flow
C_{xy}	Covariance function
CV	Coefficient of variation
d	Characteristic plant diameter
Δz	Leaf ridge height
δ	Viscous sublayer height
δ^+	Normalised height of the viscous sublayer
DMD	Drag measurement device
E	'Tension' Young's modulus
E_b	'Bending' Young's modulus
EI	Flexural rigidity
f	Frequency
f_s	Sampling frequency
F	Mean drag force
F_m	Total mean drag force (i.e., tip + leaf)
$\hat{F}_m$	Instantaneous total drag force (i.e., tip + leaf)

I. Albayrak (✉)
Laboratory of Hydraulics, Hydrology and Glaciology (VAW),
ETH Zurich, Wolfgang-Pauli-Str. 27, 8093 Zurich, Switzerland
e-mail: albayrak@vaw.baug.ethz.ch

V. Nikora
School of Engineering, Fraser Noble Building, University
of Aberdeen, Aberdeen AB24 3UE, UK

O. Miler
Leibniz-Institute of Freshwater Ecology and Inland Fisheries,
Müggelseedamm 301, 12587 Berlin, Germany

M. T. O'Hare
Centre for Ecology and Hydrology Edinburgh, Bush Estate,
Penicuik, Midlothian EH26 0QB, UK

F_t	Mean drag force acting on the rod tip
$\hat{F}_t$	Instantaneous drag force acting at the rod tip
h	Water depth
h_i	Height of the lateral projection of plant
I	Second moment area
K_d	Kurtosis coefficient
L	Leaf, stem or shoot length
L_f	Length of plant lateral projection
LFTF	Leaf force transfer function
LBL	Leaf boundary layer
LVTF	Leaf velocity transfer function
$MR_{\hat{F}_m u_d}$	Average of maximum cross-correlation coefficients between drag force and downstream velocity
$MR_{u_a \hat{F}_m}$	Average of maximum cross-correlation coefficients between approach velocity and drag force
$MR_{u_a u_d}$	Average of maximum cross-correlation coefficients between approach velocity and downstream velocity
n	Number of samples
PSD	Power spectral density
Q	Discharge
R_{xy}	Cross-correlation function
$R_{\hat{F}_m U_d}$	Cross-correlation function between drag force and downstream velocity
$R_{u_a \hat{F}_m}$	Cross-correlation function between approach velocity and drag force
$R_{u_a u_d}$	Cross-correlation function between approach and downstream velocities
Re	Reynolds number
Re_h	Depth-based Reynolds number
Re_L	Plant length-based Reynolds number
Re_{Lc}	Critical Reynolds number for transition from laminar boundary layer to the turbulent boundary layer
ρ	Fluid density
σ_d	Standard deviation of drag force
σ_{u_a}	Standard deviation of approach velocity
σ_{u_d}	Standard deviation of the downstream velocity
σ_m^2	Total variance of drag force
σ_t^2	Variance related to the rod tip
$\sigma_{u_a}^2$	Variance of approach velocity
S_b	Flume bed slope
S_d	Skewness coefficient
$S_{\hat{F}_m}$	Power spectral density of drag force
S_{u_a}	Power spectral density of approach velocity
S_{u_d}	Power spectral density of downstream velocity
SFTF	Shoot force transfer function
SVTF	Shoot velocity transfer function
STFTF	Stem force transfer function
STVTF	Stem velocity transfer function

t	Time
τ	Time lag
τ_0	Mean shear stress at a leaf surface
u	Instantaneous longitudinal velocity
u'	Fluctuating component of longitudinal velocity
u_*	Friction velocity
U	Time-averaged longitudinal velocity
U_a	Time-averaged velocity in front of a shoot or its parts
U_f	Undisturbed velocity integrated over A_f
U_i	Undisturbed velocity integrated over h_i
U_m	Cross-sectional average velocity
υ	Fluid kinematic viscosity
z^+	Leaf ridge Reynolds number
$\overline{z^+}$	Average z^+

Introduction

The forms and functions of aquatic plants are diverse and reflect complex multi-scale non-linear interactions between biological, biophysical, and biochemical processes (Jumars et al. 2001; Dodds 2002). These interactions are of great importance for river hydrodynamics and ecology, including sediment transport, mixing, hydraulic resistance, and the overall performance of river ecosystems. In spite of some recent progress towards better understanding of these interactions, there are still many gaps in current knowledge, particularly related to drag-generating and drag-control mechanisms and potential effects of plant biomechanics (Ennos 1999; Koehl 1999; Boller and Carrington 2006; O'Hare et al. 2007). Freshwater plants in unidirectional benthic boundary layers such as rivers and streams experience drag forces imposed by flowing water at a range of scales such as patch mosaic, patch, plant, shoot, stem, and leaf scales (Nikora 2010). The biophysical processes at these scales are likely to be interconnected, together determining the total drag force which can be considered as a superposition of viscous friction at the water-plant interfaces and form drag often associated with flow separation. To enhance performance and to avoid breakage or uprooting under high flow loads, plants need to minimise the total drag F that often can be parameterized as:

$$F = 0.5 \rho C_d A U^2 \tag{1}$$

where U is a reference flow velocity, ρ is fluid density, A is a reference area, and C_d is a drag coefficient. The total drag F can be minimised by utilising two mechanisms: (I) reduction of the effective plant surface area A (e.g., by folding leaves and/or coalescing leaves around stems in response to increasing velocity during a flood); and/or (II) shape reconfiguration that makes plants streamlined and/or

waving that prevents or reduces flow separation and minimises the drag coefficient C_d (Usherwood et al. 1997; Nikora 2010).

In general, we can distinguish two types of reconfiguration, static and dynamic. Static reconfiguration is the change of a plant shape in response to the changing velocity without involvement of waviness or flutter. Leaves folding and plant shape streamlining represent examples of the static reconfiguration. Dynamic reconfiguration is a result of non-linear interactions leading to the appearance of flutter or travelling waves constantly changing a plant shape even at a fixed flow velocity (Usherwood et al. 1997; Nikora 2010). Static and dynamic reconfigurations in response to increasing flow velocity often lead to deviation from a quadratic relationship between the drag and flow velocity (Vogel 1989, 1994, 2009; Zhu and Peskin 2002, 2007; Sand-Jensen 2003; Alben et al. 2004; Armanini et al. 2005; Statzner et al. 2006). Vogel (1989, 1994) expressed this effect in terms of an exponent α (known as the Vogel exponent) noting that the drag force scales with an approach velocity, in general, as $U^{2+\alpha}$. If a body is rigid and the Reynolds number (Re) is high, the drag force scales as $F \sim U^2$ (i.e., $\alpha = 0$), while for a flexible body it is often observed that $\alpha < 0$, meaning that the product of a plant area A with a drag coefficient C_d decreases with increasing velocity (Vogel 1989). Indeed, experiments with live plants show that at high Re freshwater plants often exhibit $\alpha \approx -1$ (Sand-Jensen 2003). Although many experimental studies have focused on the reconfiguration of plants in flowing water or air and on the scaling of drag force with flow velocity (Fathi-Moghadam and Kouwen 1997; Oplatka 1998; Sand-Jensen 2003; Armanini et al. 2005; Vollsinger et al. 2005; Xavier et al. 2010), the theoretical and physical interpretations of this phenomenon are still needed, especially concerning flow–plant interactions at leaf, stem, and shoot scales and interrelations between these scales (Järvelä 2002; Wilson et al. 2003).

Some useful analogies for flow-plants considerations can be found in studies of a simple case of a flexible fiber in a 2D flow. For such a system, Alben et al. (2002, 2004) concluded that as a consequence of the fluid force domination over the elastic bending force of the fiber, the drag scaling of the fiber changes from the classic rigid body scaling $F \sim U^2$ to a different scaling $F \sim U^{4/3}$. Zhu and Peskin (2002, 2007) reported a numerical study of one-dimensional flag in a 2D viscous flow and found that: (1) a flexible flag experiences a drag reduction compared to the rigid one, (2) bending rigidity significantly influences the drag force, and (3) drag coefficient decreases with increasing non-dimensional flag length. In addition, recent numerical work of Zhu (2008) also revealed a certain Reynolds number effect, with the drag–velocity scaling exponent decreasing from 2 to 4/3 as Re increases. These

findings for 2D bodies can be supplemented with those for more realistic cases of 3D shapes. Schouveiler and Boudaoud (2006), motivated by Vogel's (1989) work, investigated the mechanisms of reconfiguration of circular plastic sheets cut along radius, considered as models of broad leaves subjected to a wind force in a uniform flow. They found that increasing velocity causes rolling up of the plastic sheets into the cones leading to a decline in the drag coefficient. Gosselin et al. (2010) suggested a more general approach to explain the drag reduction of flexible plates via reconfiguration. They found that all experimental data collapse onto a single curve if presented in dimensionless form using the reconfiguration number (that characterises the effect of flexibility on drag) and the Cauchy number (that characterises the deformation of an elastic plate under the effect of flow). Also, based on an empirical drag formulation, a simple reconfiguration model for the flexible plates was proposed. This approach was further extended by Luhar and Nepf (2011) who considered a more complex case involving buoyancy effects. On the other hand, Albayrak et al. (2012) studied flow–plant interactions at a leaf scale with an emphasis on the effects of leaf shape, serration, roughness and flexural rigidity on the drag force. Leaf shape was found to be the most important factor determining flow–leaf interactions, with flexural rigidity, serration and surface roughness affecting the magnitude of this factor. So far, the possible physical mechanisms of drag control by terrestrial and aquatic plants were investigated by using idealized systems in uniform flows (i.e., flexible fibers, plates, circular flexible sheets and artificial leaf models), and typically neglecting the turbulence effects. However, many aquatic plants often live in highly turbulent flows. Furthermore, compared to simple systems, plants also exhibit much more complex multi-scale hierarchical morphology that require additional factors such as scale interconnections, porosity, and mutual interferences to be taken into consideration.

The main objective of this study is therefore to provide new information on the biophysics of flow–plant interactions at leaf, stem and shoot scales. The main focus is on the four key interconnected facets of these interactions: (1) bulk statistics, spectral characteristics, and correlations of drag force and flow velocity, (2) physical drag control mechanisms at each scale, (3) the effects of leaf, stem and shoots morphologies and biomechanical properties on plant reconfiguration; and (4) the potential implications of leaf and shoot reconfigurations for the adaptation of macrophytes to different hydraulic habitats. These matters are addressed using a series of synchronous drag force and velocity measurements as well as high resolution video recordings in well-controlled experiments with leaves, stems and shoots of the common freshwater marginal plant species *Glyceria fluitans* (L.) R. Br.

Materials and methods

In this section, we describe the facilities and experimental setup, the measurement devices, plant characteristics, the experimental procedure, and statistical parameters used in data analyses.

Facilities and experimental setup

Experiments were conducted in a glass sided flume (12.5 m long, 0.3 m wide, and 0.45 m deep) in the Fluid Mechanics Laboratory of the University of Aberdeen (Fig. 1). The experimental matrix included seven different flow rates at a constant water depth $h = 0.20$ m, with the bed slope adjusted for each run in order to obtain (quasi-) uniform flow conditions (Table 1). The measurements were carried out 8 cm below the water surface within the flume section 5.3–6 m from the flume entrance, where the flow field was fully developed with a nearly homogeneous vertical profile of the mean longitudinal velocity within a 12–13 cm thick upper layer. Table 1 presents key background hydraulic parameters. In Table 1, the 'plant' Reynolds number Re_L is based on the approach velocity U_a (at a leaf level) and leaf, stem or shoot length L (see the "data processing and analysis"), and the 'depth' Reynolds number Re_h is based on the cross-sectional average velocity U_m and the flow depth h, i.e.:

$$Re_L = U_a L / \upsilon \tag{2}$$

$$Re_h = U_m h / \upsilon \tag{3}$$

where υ is fluid kinematic viscosity.

Measurement devices

Drag measurement device (DMD)

The mean and fluctuating drag forces acting on a leaf, stem or shoot were measured using the drag measurement device (DMD) described in detail in Albayrak et al. (2012). The DMD consists of a load cell, an elliptic shaped brass tube, and a stainless steel rod attached to the load cell as an extension of the beam (Fig. 1b). The rod is placed vertically in the center of the brass tube. A shoot or its components (e.g. stem or leaf) can be easily attached to the tip of the rod using super-glue. Any force applied along the flow direction to the rod and an attached shoot creates a rod/beam deflection which is proportional to a voltage signal. The DMD allows measuring small forces (*mN*) at a sampling frequency from 1 to 1,000 Hz. The DMD was calibrated by applying a series of known weights to the rod tip and measuring the output voltages. The calibrations were routinely carried out before and after each experiment.

Acoustic Doppler velocimeters (ADVs)

Three components of in-front (approach) and behind-plant velocities were measured using two Acoustic Doppler velocimeters (ADVs) at 8 cm below water surface (Fig. 1a). The upstream ADV was placed 60 cm away from the submerged tube of the DMD in order to measure the approach velocity and turbulence characteristics of the undisturbed flow and the downstream ADV was placed 5 cm away from the back tip of plant components to measure velocity and turbulence characteristics in the wake region.

Table 1 Background hydraulic parameters for the experiments

h (m)	Q (m³/s)	U_m (m/s)	S_b	Re_h	Re_L
0.20	0.012	0.20	0.001	0.4×10^5	$(0.3–1.3) \times 10^5$
0.20	0.018	0.30	0.001	0.6×10^5	$(0.5–1.8) \times 10^5$
0.20	0.024	0.40	0.001	0.8×10^5	$(0.7–2.5) \times 10^5$
0.20	0.030	0.50	0.002	1.0×10^5	$(0.9–3.0) \times 10^5$
0.20	0.036	0.60	0.002	1.2×10^5	$(1.0–3.6) \times 10^5$
0.20	0.042	0.70	0.004	1.4×10^5	$(1.3–4.3) \times 10^5$
0.20	0.048	0.80	0.004	1.6×10^5	$(1.5–4.9) \times 10^5$

h water depth, Q water discharge, U_m cross-sectional average velocity, S_b bed slope, Re_h depth Reynolds number, Re_L plant Reynolds number

Fig. 1 **a** A sketch of the measurement section and the positions of ADV, DMD and Camera, **b** a picture of the DMD
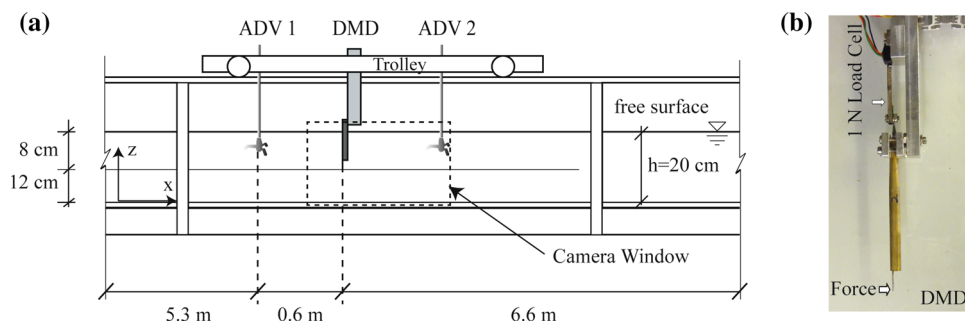
Table 2 Plant leaf, stem and shoot morphological and biomechanical characteristics

Expr. code	Leaf/stem/ shoot	Length, L (m)	Wetted area, A_w (m^2)	Second moment area, I (m^4)	Young's modulus, E (N/m^2)	Flexural rigidity $EI = E * I$ in N*m^2	Mean width B (m)	Aspect ratio (L/B)
S1L1	Leaf	0.22	0.0022	3×10^{-15}	27.5×10^6	8.2×10^{-8}	0.50×10^{-2}	44
S1L2	Leaf	0.27	0.0028	4×10^{-15}	24.4×10^6	9.8×10^{-8}	0.52×10^{-2}	52
S1L3	Leaf	0.33	0.0036	4.1×10^{-15}	23.7×10^6	9.6×10^{-8}	0.54×10^{-2}	61
S1ST	Stem	0.58	0.0050	6.0×10^{-12}	15.7×10^6	94.6×10^{-6}	0.35×10^{-2}	165
S1WS	Whole shoot	0.65	0.0137					
S2L1	Leaf	0.24	0.0022	2.4×10^{-15}	75.4×10^6	18.4×10^{-8}	0.46×10^{-2}	52
S2L2	Leaf	0.25	0.0026	3.4×10^{-15}	40.9×10^6	13.9×10^{-8}	0.52×10^{-2}	48
S2L3	Leaf	0.30	0.0032	3.5×10^{-15}	39.5×10^6	14×10^{-8}	0.53×10^{-2}	57
S2L4	Leaf	0.32	0.0029	2.2×10^{-15}	41.5×10^6	9.2×10^{-8}	0.45×10^{-2}	71
S2ST	Stem	0.27	0.0023	10.3×10^{-12}	28.3×10^6	290×10^{-6}	0.40×10^{-2}	67
S2WS	Whole shoot	0.61	0.0132					
S3L1	Leaf	0.29	0.0044	15.1×10^{-15}	20.7×10^6	31.2×10^{-8}	0.76×10^{-2}	38
S3L2	Leaf	0.29	0.0043	14.1×10^{-15}	30.5×10^6	38.4×10^{-8}	0.74×10^{-2}	39
S3L3	Leaf	0.31	0.0041	10.5×10^{-15}	36.3×10^6	37.0×10^{-8}	0.66×10^{-2}	47
S3L4	Leaf	0.40	0.0043	3.9×10^{-15}	37.1×10^6	13.4×10^{-8}	0.54×10^{-2}	74
S3L5	Leaf	0.18	0.0018	2.6×10^{-15}	39.5×10^6	10.2×10^{-8}	0.50×10^{-2}	36
S3ST	Stem	0.36	0.0021	3.7×10^{-12}	40.7×10^6	151×10^{-6}	0.31×10^{-2}	117
S3WS	Whole shoot	0.79	0.0209					
S4L1	Leaf	0.25	0.0029	6.2×10^{-15}	46.7×10^6	29.3×10^{-8}	0.58×10^{-2}	43
S4L2	Leaf	0.29	0.0032	3.2×10^{-15}	48.0×10^6	15.2×10^{-8}	0.55×10^{-2}	53
S4L3	Leaf	0.44	0.0038	2.0×10^{-15}	51.8×10^6	10.2×10^{-8}	0.43×10^{-2}	102
S4ST	Stem	0.21	0.0015	3.2×10^{-12}	24.2×10^6	78.7×10^{-6}	0.35×10^{-2}	60
S4WS	Whole shoot	0.65	0.0132					
S5L1	Leaf	0.26	0.0039	12.9×10^{-15}	20.9×10^6	26.9×10^{-8}	0.75×10^{-2}	35
S5L2	Leaf	0.47	0.0052	5.8×10^{-15}	37.9×10^6	22.1×10^{-8}	0.55×10^{-2}	85
S5L3	Leaf	0.48	0.0044	2.1×10^{-15}	54.4×10^6	11.7×10^{-8}	0.46×10^{-2}	104
S5ST	Stem	0.34	0.0018	10.3×10^{-12}	13.45×10^6	138.4×10^{-6}	0.40×10^{-2}	85
S5WS	Whole shoot	0.81	0.0153					
S6WS	Whole shoot	0.62	0.0112	N/A	N/A	N/A		
S7WS	Whole shoot	0.50	0.0082	N/A	N/A	N/A		

Video recording

For the visualization of flow–plant interactions, a full-HD progressive scanning camera with a frame size of 1920 × 1080 pixels (*Width* × *Height*) and a frame rate of 25 *fps* was used in all experiments to perform video recordings of a 40 cm by 30 cm sampling window (or a larger area if the size of the plant components exceeded a standard window, Fig. 1a). Video data were analyzed to obtain qualitative information on plant component motions at different flow velocities in relation to plant reconfiguration at different scales.

Plants characteristics

Glyceria fluitans, chosen for this study, is a semi-aquatic plant species. It is adapted to survive and grow in slow to moderate flowing streams and river margins (typical flow velocity ~ 0.40 m/s, Preston and Croft 2001). The leaves of *G. fluitans* are positioned horizontally when submerged and have a strap-like shape. A total of seven *G. fluitans* shoots varying in size were sampled from a burn at the Leith Hall Estate in Kennethmont/Aberdeenshire, Scotland, UK. All shoots were stored in a 50 L circular flow-through aquarium with aeration where they were kept under a 15:9 h day:night cycle at 15 °C for a maximum of 1 week. The apical growth region of a *G. fluitans* shoot is located at the tip of the shoot so that the leaves closer to the shoot's root are older than those closer to the tip. The shoots were denoted as S1, S2, S3, S4, S5, S6 and S7 (Table 2). In the experiments, the following naming system was used: shoot (S) number and then leaf (L) number, stem (ST) number or whole shoots (WS). As an example,

Fig. 2 Images of **a** shoot 4 (S4WS) and **b** its third leaf (S4L3) and **c** stem (S4ST)
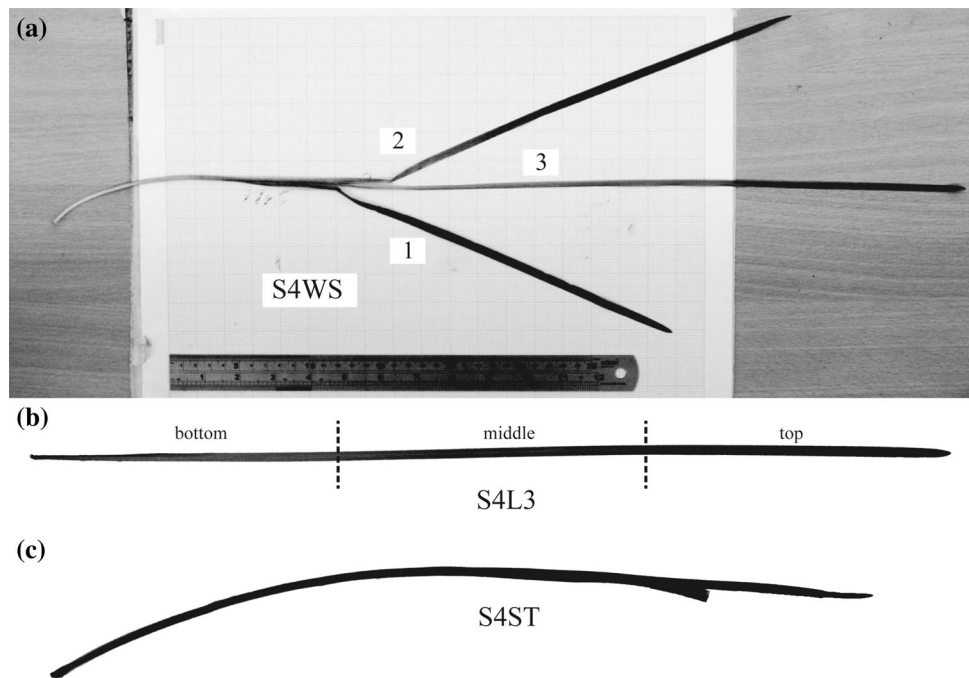
the third leaf of the fourth shoot was named as S4L3 (Fig. 2).

The biomechanical properties of the bottom, middle and top sections of leaves (Fig. 2b) and stems of *G. fluitans* were measured after the drag and velocity measurements of shoot, stem and leaves were completed. Using an image analysis technique, the wetted areas, diameters/widths, and lengths of shoots, stems and leaves were calculated from the high resolution pictures taken with a camera (Fuji FinePix S1000fd, Fujifilm, Tokyo, Japan) on a light table (Table 2). Cross-sectional slices of leaves and stems with a thickness thinner than 1 mm were cut with a razor blade and pictures of cross-sections were taken under a microscope using a digital camera. These images were used to calculate the cross-sectional areas (Table 2). To analyse the resistance of the plant leaves and stems against tension forces and to quantify their flexibility under bending, we performed uniaxial tension tests. In the tension tests, the 'tension' Young's modulus E, as a measure of the ability of a material to withstand changes in length under uniaxial tension, was measured. The tension tests were performed with a Hounsfield S-series bench top testing machine Model H10K-S UTM using a 100 N load cell.

The flexural rigidity EI, which is a measure of the object overall flexibility, was calculated as the product of 'tension' Young's modulus E and the second moment of area I. The latter was obtained from cross-section measurements of stems and leaves (Miler et al. 2012). Since plant parts, especially the leaves, were too flexible for the 100 N load cell used in the biomechanical experiments, we could not perform bending tests and thus used the 'tension' Young's

modulus E rather than the 'bending' Young's modulus E_b. Note that the estimates of the Young's modulus from tension and bending tests may be different, in general, due to material heterogeneity and anisotropy. More details on the techniques employed can be found in Miler et al. (2012).

Experimental procedure

For each of the 7 shoots, 4 stems and 18 leaves (Table 2), velocity and drag force measurements as well as video recordings were carried out with synchronized ADVs ($f_s = 50$ Hz), DMD ($f_s = 50$ Hz) and full-HD camera ($f_s = 25$ Hz) for 5 min at seven different flow rates (Table 1). Whereas the morphological and biomechanical characteristics of the stem of the shoot 4 (S4ST) were presented in the table, the drag force and velocity measurements for this stem could not be carried out due to a technical problem and hence this particular stem will not be considered in the data analysis. In a typical test run, a plant shoot (stem, leaf) was glued to the tip of the steel rod of the DMD and then the drag force measured by the DMD was set to zero in a still water tank where the shoot was located 8 cm below the water surface. Second, the DMD was positioned in the center of the flume between the two ADVs as shown in Fig. 1a. The measurements started with the whole shoot and then were repeated with its stem and each leaf, which were carefully detached from the already tested shoot. To assess the contributions of the DMD rod to the obtained force estimates, the measurements have been also conducted without plant parts attached to the DMD tip.

Data processing and analysis

Drag and velocity data: bulk statistics

In the drag data analysis, the rod contributions to the mean measured drag and its variance were subtracted. The mean drag force F acting on a shoot or its components (i.e., leaves and stems) was computed as:

$$F = F_m - F_t, F_m = \frac{1}{n} \sum_{i-1}^{n} \hat{F}_{m_i} \quad \text{and} \quad F_t = \frac{1}{n} \sum_{i-1}^{n} \hat{F}_{t_i} \quad (4)$$

where F_m is the total mean (i.e., time-averaged) drag force (i.e., tip + leaf), F_t is the mean drag force acting on the rod tip, $\hat{F}_m$ and $\hat{F}_t$ are the instantaneous total drag force and the instantaneous drag force at the rod tip, respectively, and $n = 15,000$ is the number of samples within a measurement time period (i.e., the number of recorded data points). The standard deviation (σ_d) of the instantaneous drag force was calculated as:

$$\sigma_d = \sqrt{\sigma_m^2 - \sigma_t^2}, \sigma_m^2 = \frac{1}{n} \sum_{i=1}^{n} \left(\hat{F}_{m_i} - F_m\right)^2 \text{ and}$$

$$\sigma_t^2 = \frac{1}{n} \sum_{i=1}^{n} \left(\hat{F}_{t_i} - F_t\right)^2 \quad (5)$$

where σ_m^2 and σ_t^2 are the total variance and the variance related to the rod tip, respectively. F_t, $\hat{F}_t$ and σ_t^2 were determined in separate measurements (i.e., without attached plant elements) at the investigated range of flow velocities. The coefficient of variation CV, skewness coefficient S_d and kurtosis coefficient K_d were calculated using Eqs. (4) and (5):

$$CV = \sigma_d/F, S_d = \left(\frac{1}{n} \sum_{i=1}^{n} \left(\hat{F}_{m_i} - F_m\right)^3\right)/\sigma_d^3 \text{ and}$$

$$K_d = \left(\frac{1}{n} \sum_{i=1}^{n} \left(\hat{F}_{m_i} - F_m\right)^4\right)/\sigma_d^4 - 3 \quad (6)$$

where it is reasonably assumed that the contributions from the rod tip to the skewness and kurtosis coefficients are negligible, as evident from preliminary estimates. The drag coefficient, C_d as a function of Reynolds number, Re_L (see Eq. 2) was calculated following a conventional approach, i.e.:

$$C_d = 2F/\left(\rho A_w U_a^2\right) \quad (7)$$

where F is the mean drag force, A_w is the total wetted area, and U_a is the time-averaged velocity measured in front of a shoot or its parts (i.e., leaves or stem), ρ is fluid density. The parameterization of C_d and Re_L depends on choices in the definition of the reference plant area, velocity and length of a plant (Vogel 1994; Statzner et al. 2006).

Table 3 Reference area, velocity and length defined by three approaches for freshwater macrophytes (Statzner et al. 2006)

	Most dynamic, traditional	Intermediate	Most static
Reference area	A_f: frontal projection area of plant (m²)	A_i: characteristic plant diameter (d) x height (h_i) of the lateral projection of plant (m²)	A_w: total wetted surface area of plant (m²)
Reference velocity	U_f: undisturbed velocity integrated over A_f (m/s)	U_i: undisturbed velocity integrated over h_i (m/s)	U_a: uniform undisturbed velocity (m/s)
Reference length	L_f: length of the lateral projection of plant (m)	L_f: length of the lateral projection of plant (m)	L: shoot length of plant (m)

Statzner et al. (2006) reviewed and compared three approaches (most dynamic/traditional, intermediate, and most static) involving the choices suggested by Sand-Jensen (2003), Green (2005) and Sukhodolov (2005) (Table 3). Statzner et al. (2006) concluded that the traditional approach provides the most comprehensive parameterization of drag forces on freshwater macrophytes. However, due to the limitations in our experimental setup, the variables for applying this approach were not measured. Instead, the variables for the most static approach (Sand-Jensen 2003) were measured with high accuracy and used in the data analysis.

Bulk statistics (mean, standard deviations, CV, skewness, and kurtosis) were also obtained for the velocity time series measured with the upstream and downstream ADVs. Equations used are similar to (4) to (6). As a preliminary step, the measured instantaneous longitudinal velocity u was de-spiked (Goring and Nikora 2002) before obtaining its fluctuating component u', i.e.:

$$u' = u - U \quad (8)$$

where u denotes the instantaneous velocity, and U denotes the mean (time averaged) velocity in the longitudinal direction.

Spectra and drag–velocity correlations

The power spectral densities (PSD) of the drag force and velocities were obtained, employing a Matlab pwelch-function, as smoothed squared fast Fourier transforms of the time series. Then, the computed PSDs were used to estimate the shoot (SVTF, SFTF), stem (STVTF, STFTF), and leaf (LVTF and LFTF) velocity and drag force transfer functions as, for example, for SVTF and SFTF:

$$SVTF(f) = \frac{S_{u_d}}{S_{u_a}} \quad \text{and} \quad SFTF(f) = \frac{S_{\hat{F}_m}}{S_{u_a}} \tag{9}$$

where S_{u_a}, S_{u_d}, and $S_{\hat{F}_m}$ are the power spectral densities of the measured approach and downstream velocities, and the drag force, respectively. Note that the contributions from the rod tip PSDs to the total measured drag PSDs are negligible. Indeed these contributions to the variance range only from 0.2 to 3 % while the tip's PSD amplitudes are at least one order of magnitude lower compared to the PSD amplitudes of the total drag. The transfer functions STVTF, STFTF, LVTF and LFTF were computed similar to Eq. (9). The velocity and drag force transfer functions for a shoot, stem or leaf are measures of the (linear) relationship between the output (e.g., drag) and input (e.g., approach velocity) signals in the frequency domain. In addition, the cross-correlation functions (i.e., normalized cross-covariance functions) $R_{xy}(\tau)$ were also calculated as:

$$R_{xy}(\tau) = \frac{C_{xy}(\tau)}{\sigma_x \sigma_y},$$

$$C_{xy}(\tau) = \frac{1}{n - \tau/\Delta t} \sum_{i=1}^{i=n-\tau/\Delta t} (x_i - \bar{x})(y_{i+\tau/\Delta t} - \bar{y}) \tag{10}$$

where $C_{xy}(\tau)$ is the covariance function between mean-removed time series $x(t)$ and $y(t)$, τ is a time lag, Δt is the sampling interval, x and y denote drag and/or velocities, and an overbar defines time-averaging. The function $R_{xy}(\tau)$ measures the degree of (linear) dependence between $x(t)$ and $y(t)$ at a time lag τ in $y(t)$ relative to $x(t)$. Using Eq. 10, we calculated the cross-correlation functions between the approach and downstream velocities, $R_{u_a u_d}(\tau)$, the approach velocity and the drag force, $R_{u_a \hat{F}_m}(\tau)$, and the drag force and the downstream velocity, $R_{\hat{F}_m u_d}(\tau)$.

Results

Leaf experiments

Bulk statistics of drag force

The time-averaged drag forces F experienced by 18 studied leaves are shown in Fig. 3a as a function of the mean upstream velocity U_a, together with power-type fitting curves. At low velocities, the drag forces acting on the leaves are small and not much different, but with increasing flow velocity the differences between leaves grow. Leaf S5L2, as one of the longest leaves with the largest surface area, has the largest drag force; the shortest leaf (S3L5) with the smallest wetted area experienced the least drag force. The drag–velocity relationships are well approximated by power–type functions $F \sim U_a^{2+\alpha}$. However, the exponents $(2 + \alpha)$ are significantly less than 2 being between 1.3 and 1.75 (i.e., Vogel number $\alpha = -0.25$ to -0.70), which is typical for flexible bodies. This deviation from a rigid body behavior reflects the ability of flexible leaves to react to the increased flow forces. To identify the effects of leaf biomechanical properties, we suppressed leaf size effect by normalizing the drag force with leaf length. Figure 3b clearly reveals the strong effect of leaf flexural rigidity on the normalised drag force. Indeed, less flexible older leaves (S3L1, S4L1, and S5L1) experience the highest drag per unit length followed by medium flexible leaves. Young and very flexible leaves have the least drag per unit length. Separation of drag–velocity curves in Fig. 3b with increase in velocity indicates a growing effect of flexural rigidity. One should note that a few leaves (S3L2, S3L3, S2L1 and S1L2) do not follow this trend, which can be attributed to (I) morphological differences between leaves (i.e. aspect ratios, damage on the leaf tissue), (II) possible errors occurring in the biomechanical tests and (III) overlapping between the age groups.

The curves $C_d = f(\text{Re}_L)$ for all leaves as well as those for laminar and turbulent flat plate boundary layers are shown in Fig. 4a. The drag coefficients of laminar (C_{d-FPL}) and turbulent (C_{d-FPT}) flat plate flows are calculated as (Schlichting and Gersten 2000):

$$C_{d-FPL} = 1.328/\sqrt{\text{Re}_L} \quad \text{and} \quad C_{d-FPT} = 0.031/\sqrt[7]{\text{Re}_L}. \tag{11}$$

Note that Eq. (11) does not include the aspect-ratio (i.e., length/width ratio) effect of a plate. However, Elder (1960) found that the conventional relationships obtained by ignoring the aspect ratio effect could still give a good estimate of the total drag of any finite plate, as the plate aspect ratio effect accounts for less than ±1 % of the total drag. The measured C_d-values show a high variability among the leaves at small Re_L. This scatter in the data reflects the sensitivity of C_d-values to the leaf vertical orientation due to buoyancy and leaf biomechanics and morphology. These effects are particularly pronounced at low Re_L which are associated with low drag forces. For example, at low velocities the angle of attack between the flow and a leaf may significantly deviate from zero (due to a buoyancy effect) leading to an enhanced frontal area of the leaf. With increase in velocity (i.e., drag), the angle of attack reduces to zero. Hence, the initial leaf orientation may strongly influence the drag force and drag coefficient at low velocities, with this effect disappearing with increase in velocity (Fig. 4a). Compared to the C_d-values for laminar and turbulent flat plate boundary layers, the C_d-values for leaves are much higher at small Re_L, still being two times larger than that for the rough-wall boundary layer even at high Re_L. This indicates that in addition to the
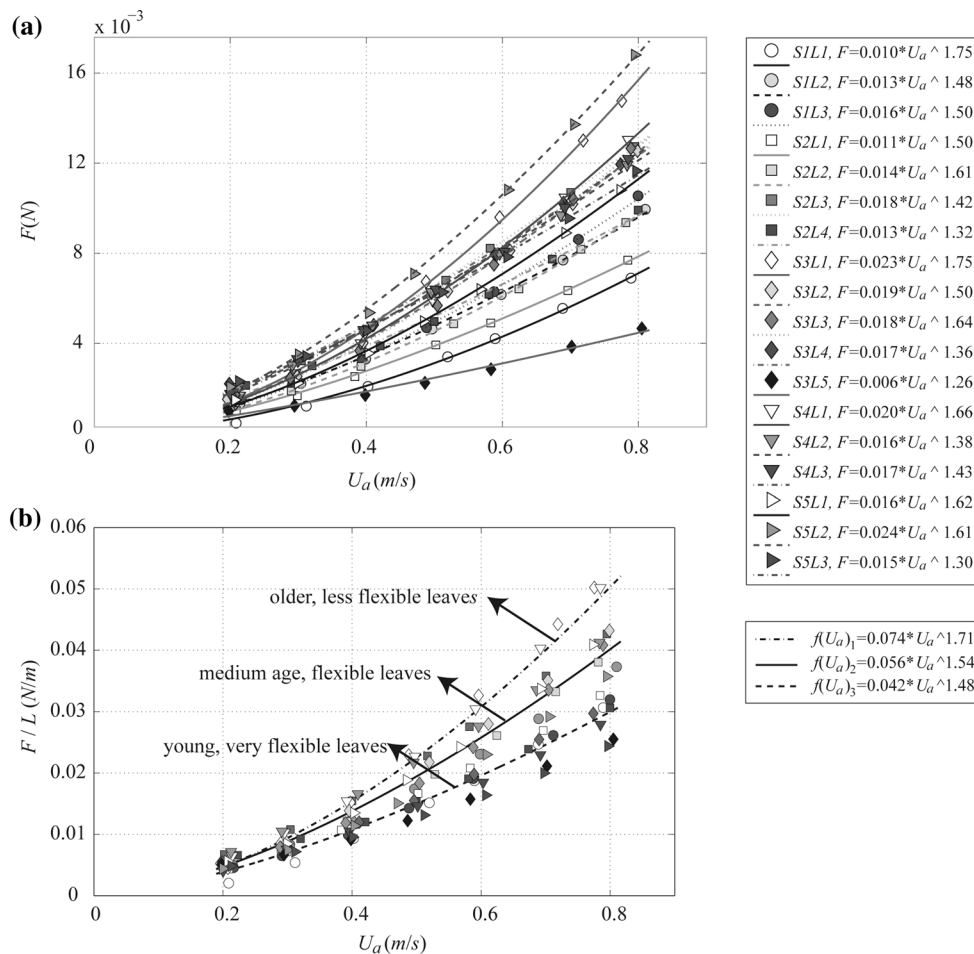
Fig. 3 Leaf drag force F (**a**) and the drag force normalized by leaf length, F/L (**b**) versus the mean approach velocity U_a

viscous (skin) friction the leaves also experience pressure drag.

Figure 4b shows the relationship between C_d and the aspect ratio L/B for all studied leaves for three velocities. The drag coefficient C_d increases with increasing L/B until L/B reaches ≈ 70. Beyond this critical point, C_d decreases with increasing L/B. In other words, beyond this certain aspect ratio, C_d of a longer leaf is less than that of a shorter one. This effect is strongest at the highest velocity. Furthermore, at each L/B the coefficient C_d decreases with increasing approach velocity.

The standard deviation σ_d of the drag force increases with increasing Re_L for all leaves, significantly diverging between the leaves at high Re_L (Fig. 4c). This divergence can be attributed to the combined effects of leaf size and their biomechanical properties, among which the flexural rigidity is likely to be a dominant factor. Indeed, younger (more flexible) leaves exhibit appreciably lower drag force variability compared to the older and more rigid leaves. A similar trend is also observed in the plot for CV (Fig. 4d).

Interestingly, at $Re_L > 10 \times 10^3$ the CV tends to a constant value of 0.07 (Fig. 4d). The drag force skewness coefficient S_d does not reveal any significant differences between the leaves, varying between -0.25 and 0.25 and being on average close to 0 (Fig. 4e). The plots of the kurtosis coefficient K_d are also similar for all leaves (Fig. 4f), with its values fluctuating around -0.10 and mostly not exceeding 0.5 in magnitude.

Turbulence effects on drag force bulk statistics

The standard deviation of the drag force σ_d for individual leaves is approximately proportional to the variance of the approach velocity $\sigma_{u_a}^2$ (Fig. 5a). This could be expected from Eq. (1) if it is written for instantaneous drag force and approach flow velocity decomposed into time-averaged and fluctuating components, i.e., $\sigma_d \approx 0.5\rho A_w C_d \sigma_{u_a}^2$. Thus, the separation of $\sigma_d = f(\sigma_{u_a})$ curves in Fig. 5a can be explained by the variability of the product $(A_w C_d)$ among
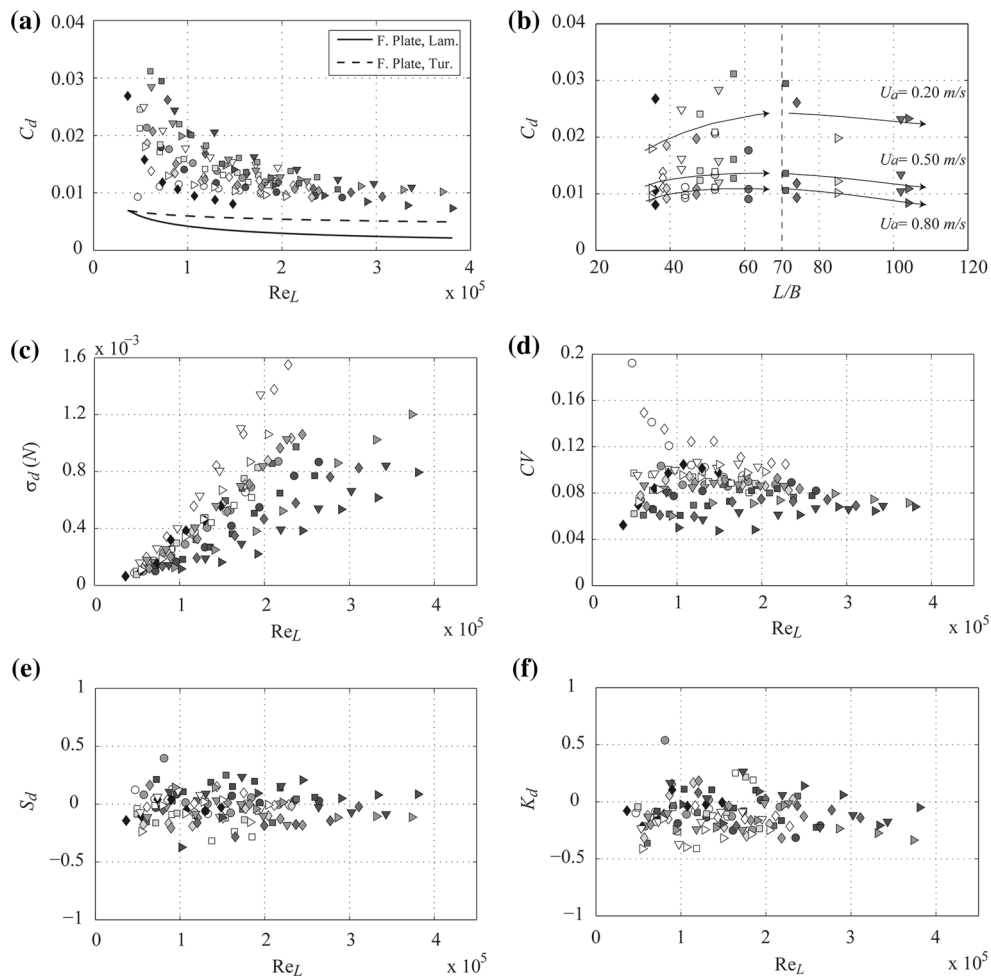
Fig. 4 The leaf drag coefficient C_d (**a**); drag standard deviation σ_d (**c**); coefficient of variation CV (**d**); skewness coefficient S_d (**e**); and kurtosis coefficient K_d (**f**) versus Reynolds number Re_L and the C_d versus aspect ratio, L/B (**b**); symbols are the same as in Fig. 3

leaves, with a clear dominance of the C_d effect that can be attributed to the differences in flexural rigidity among the leaves (Fig. 5a). The approximate relationship $\sigma_d \approx 0.5\rho A_w C_d \sigma_{u_a}^2$ predicts that $\sigma_d/\sigma_{u_a} \propto U \propto Re_L$. However, Fig. 5b highlights some concave non-linearity in the relations $\sigma_d/\sigma_{u_a} = f(Re_L)$ at high Re_L suggesting that there is a mechanism, additional to the upstream turbulence, which appears at high velocities and influences drag variability. This mechanism is likely to be related to a leaf instability that may absorb the energy of turbulent fluctuations by elastic bending and undulations (dynamic reconfiguration) resulting in reduced drag fluctuations and, thus, concave curves $\sigma_d/\sigma_{u_a} = f(Re_L)$. Comparing velocity standard deviations in front and behind a leaf one can also deduce that the leaves suppress the upstream turbulence, as evident in Fig. 5c. However, one should also keep in mind a potential role of spatial averaging by the ADV sampling volume which is difficult to properly quantify.

Spectral analysis of the drag force and flow velocity

Figure 6a shows the power spectral densities (PSD) of the approach velocity for all studied scenarios (Table 1) for S2L4. Although there is a signature of a noise floor at a high frequency range ($f > 15$ Hz), the shape of the spectra at lower frequencies is typical for open-channel flows (Nikora and Goring 2000). Velocity spectra behind the leaf (Fig. 6b) have a similar shape but lower magnitudes that is consistent with Fig. 5c, which reveals a lower turbulent energy in the leaf wake. Indeed, the leaf velocity transfer function (LVTF) shows that the approach turbulent energy is about 30–50 % higher at low frequencies and is equal to the wake turbulence energy at higher frequencies (please note that this may reflect an effect of a noise floor that in both cases is expected to be the same). This result suggests that the leaf suppresses the wake turbulent energy by 'extracting' the energy from the spectra of the approach velocities. Figure 6d shows the
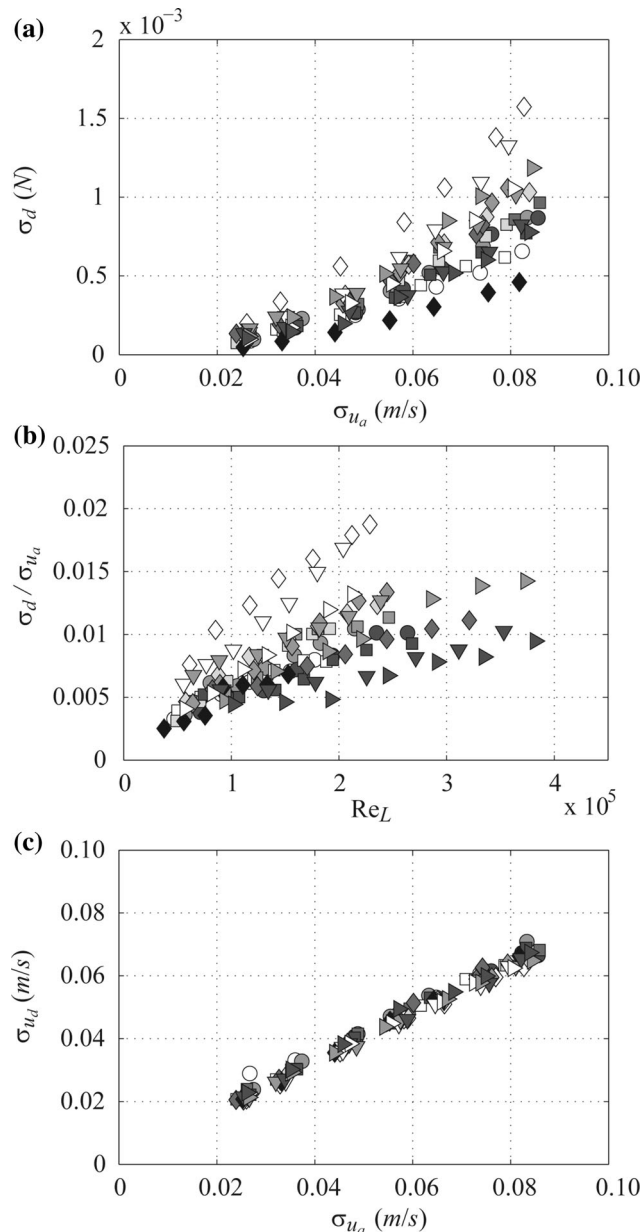
(a)

(b)

(c)

Fig. 5 The drag force standard deviation σ_d versus the standard deviation of the approach velocity σ_{u_a} (a); the ratio of σ_d to σ_{u_a} versus Re_L (b); and the standard deviation of the downstream velocity σ_{u_d} versus the standard deviation of the approach velocity σ_{u_a} (c) for all leaves; symbols are the same as in Fig. 3

spectra of the drag force for S2L4. There is a spike in the spectra at $f = 7$ Hz due to the flume vibration as well as a mild signature of a noise floor at the high frequency range for runs with $U_a < 0.50$ m/s. These features, however, are not dominant and do not mask the overall spectral shape. The slope of the drag force spectra at low frequencies follows the '−1' law as also observed in the velocity spectra. At the higher frequencies, the slope of the drag spectra is steeper than −5/3 at low velocities but tends to −5/3 with increasing approach velocity.

The leaf force transfer function (LFTF) shown in Fig. 6e reveals two frequency ranges where the LFTF exhibits elevated magnitudes or 'hills'. The positions of both LFTF hills change towards higher frequencies with increasing approach velocity, accompanied by simultaneous growth in the LFTF magnitudes. At small approach velocities, the low-frequency hill occupies frequencies between 0.2 and 0.6 Hz, which shift to the range 0.4–0.9 Hz at large velocities. The spatial equivalents of these frequencies can be obtained from the 'frozen' turbulence hypothesis as $L = U_a/f$ (Nezu and Nakagawa 1993). These spatial equivalents appear to be largely independent of the approach velocity, ranging from approximately 3–5 flow depths and exactly corresponding to the range of large-scale eddies in open-channel flows (Nezu and Nakagawa 1993). One may conclude then that the leaf response to the turbulent flow is most sensitive to large-scale turbulent eddies that represent the major part of the total turbulent energy. This low-frequency hill in the LFTF, therefore, is likely a signature of the passive interactions between flow and the leaf. The second, high-frequency, hill occurs within 1–6 Hz at small velocities changing to 4–9 Hz at high approach velocities. The spatial equivalents of these frequency ranges are also independent of the approach velocity and scale with the leaf length (from 30 to 50 % of the leaf length). It is quite plausible that this second LFTF hill is generated by the dynamic interactions between flow and the leaf.

Cross-correlations

Additional information on the flow–leaf interactions can be extracted from cross-correlation functions between approach velocity and drag ($R_{u_a \hat{F}_m}$), drag and downstream velocity ($R_{\hat{F}_m u_d}$), and the approach and downstream velocities ($R_{u_a u_d}$). Examples for experiments with leaf S2L4 are shown in Fig. 7. From the plots in Fig. 7a, b it is clear that the maximum of $R_{u_a \hat{F}_m}$ is higher than the maxima of both $R_{\hat{F}_m u_d}$ and $R_{u_a u_d}$. This means that the drag force is strongly correlated with the approach velocity highlighting the role of large-scale turbulent eddies in generating drag force fluctuations. On the other hand, $R_{\hat{F}_m u_d}$ is not much lower than $R_{u_a \hat{F}_m}$ suggesting that the leaf has a considerable effect on wake turbulence. Interestingly, the cross-correlation function $R_{u_a u_d}$ is quite small compared to $R_{u_a \hat{F}_m}$ and $R_{\hat{F}_m u_d}$ reflecting loss of correlation due to a large distance between ADV probes and, probably, the 'de-correlating' influence of a leaf. The average maxima of $R_{u_a \hat{F}_m}$ and $R_{\hat{F}_m u_d}$ i.e. $MR_{u_a \hat{F}_m}$ and $MR_{\hat{F}_m u_d}$ increase with the mean approach velocity (Fig. 7d), being consistent with behaviour of the transfer functions from the previous subsection. This effect likely reflects the role of large-scale turbulence in flow–leaf interactions, since increase in mean velocity is associated

Fig. 6 Power spectra of approach (**a**) and downstream (**b**) velocities and drag force (**d**); leaf velocity transfer (**c**) and leaf force transfer (**e**) functions for leaf S2L4
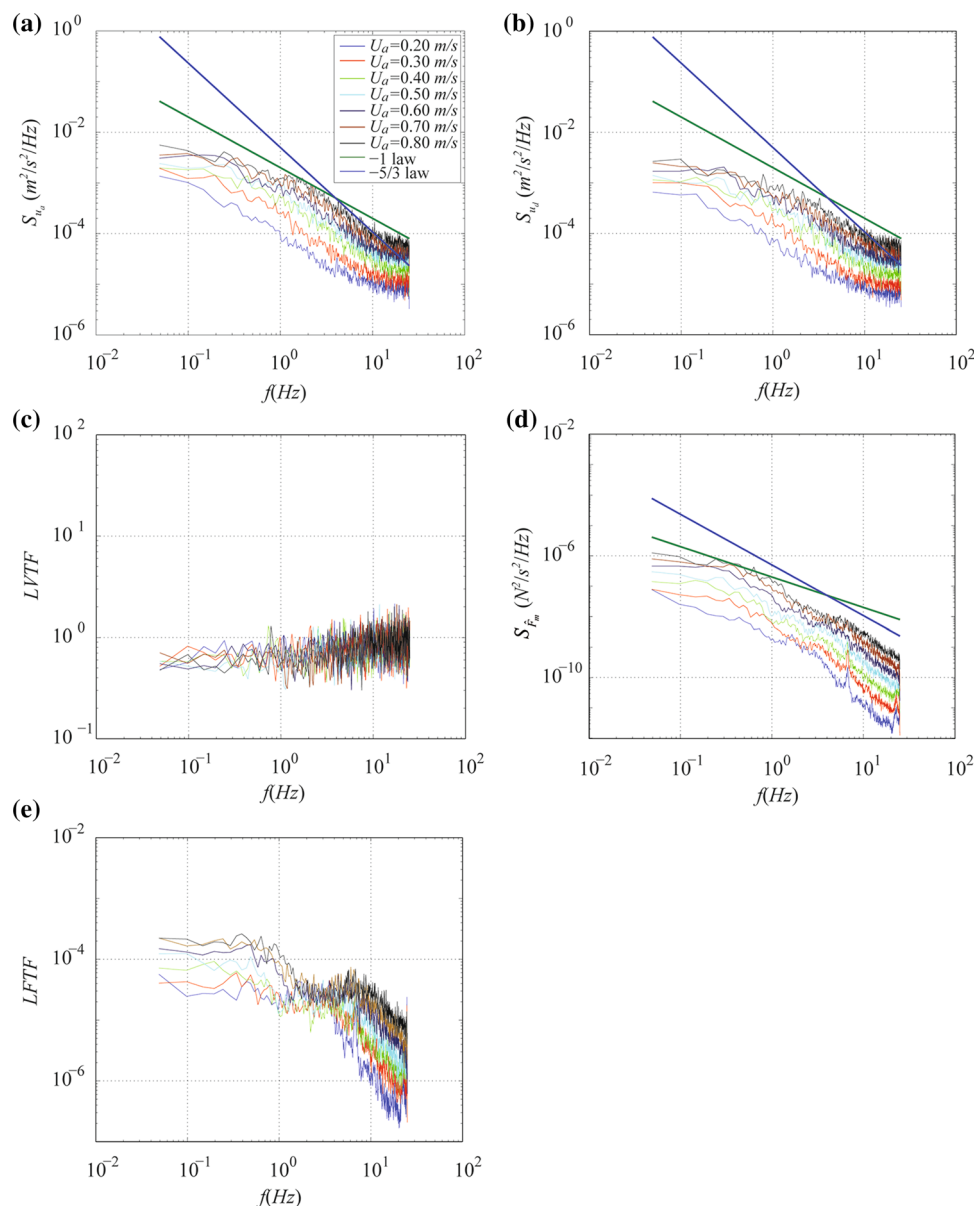

with increase in the turbulent energy of large eddies (Fig. 6a, b), which largely control drag force fluctuations.

Possible drag control mechanisms

Based on video recordings and the data analyses presented in the preceding subsections, we may speculate about several possible drag reduction mechanisms utilised by plant leaves in response to the high flow velocities. First, with increase in flow velocity the leaves bend and align with the flow by reducing the form drag (i.e., static reconfiguration mechanism, Fig. 8a). At highest velocity, leaves exhibit quick undulations which might further reduce the total drag force (i.e., dynamic reconfiguration

mechanism, Usherwood et al. 1997; Nikora 2010; Albayrak et al. 2012; Siniscalchi and Nikora 2013). This mechanism finds support in the analysis of bulk and spectral statistics of flow velocity and drag force. Another possible drag reduction mechanism may be due to the 'riblets' which are clearly seen on the *G. fluitans* leaf surface (Fig. 8b). Indeed, many studies in fluids engineering have shown that surface riblets may reduce drag due to skin-friction by 8–10 % (Walsh and Lindemann 1984; Tani 1988). Figure 8b shows, as an example, the surface and a cross-section of leaf S3L2 (a cross-section photo was taken with a microscope) that clearly demonstrates the existence of transverse ridges on the upper leaf surface. From such images, the ridge heights Δz were measured along a leaf
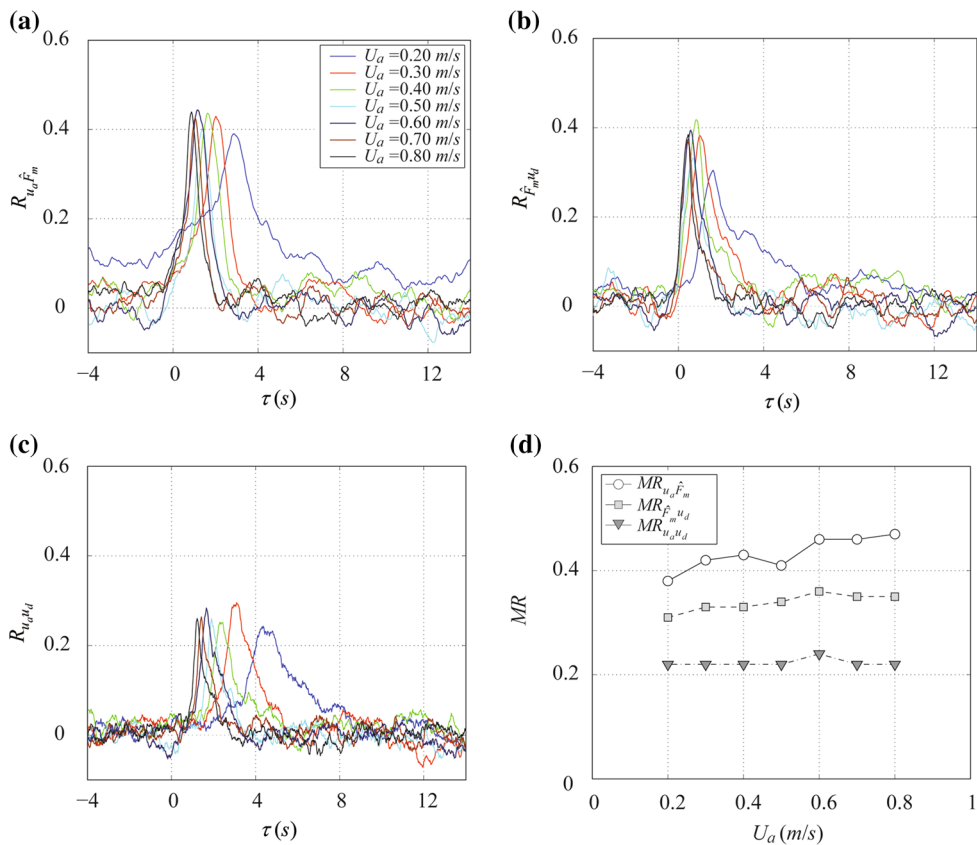
cross-section at each part of a leaf (Fig. 8b, d). Using data from the drag force measurements, we have obtained the ridge Reynolds numbers z^+ as:

$$z^+ = \Delta z u_* / \upsilon, \ u_* = \sqrt{\tau_0 / \rho} \ \text{and} \ \tau_0 = F / A_w \quad (12)$$

where u_* is the friction velocity, and τ_0 is the mean shear stress at the leaf surface. The parameter $\overline{z^+}$ is the averaged z^+ over a leaf-cross section. As one can see in Fig. 8c, the z^+ and $\overline{z^+}$ values are comparable to the normalised height of the viscous sublayer ($\delta^+ = \delta u_* / \upsilon \approx 5...10$) at the leaf surface (Fig. 8c, d) that is a known requirement for riblet drag reduction (Walsh and Lindemann 1984). δ is the vertical distance from the valley between the riblets. Figure 8b also shows that the lower leaf surface is much smoother. This difference in roughnesses between the upper and lower sides of a leaf might cause instabilities and non-linear interactions between the leaf and flow, leading to further drag reduction.

Stem experiments

Bulk statistics of drag force

The flexural rigidities of stems are about three orders of magnitude higher than those of leaves and vary from 94.6×10^{-6} up to 290×10^{-6} Nm^2, reflecting significant structural differences between them (Miler et al. 2012). Stems and leaves of *G. fluitans* also show distinct differences in their morphology, i.e., cylindrical shape for the stems vs. thin-strip shape for the leaves. Hence, one may expect that stems interact with flow in a different way. The relationships between the time-averaged drag forces and approach velocities for the four plant stems are shown in Fig. 9a, including power–type fitting curves. The performance of stems S2ST, S3ST and S5ST are approximately the same (i.e., $F \propto U_a^{2+\alpha}$ with $\alpha \approx -0.56$) while stem S1ST behaves slightly differently (i.e., $F \propto U_a^{2+\alpha}$ with $\alpha \approx -0.43$) (Fig. 9a). This difference is most likely due to a much higher length of S1ST (Table 2) and a small flexible leaf attached to its end, which could change the interaction conditions compared to the other stems.

To investigate the role of stem length, the average drag force was normalized by stem length and plotted against approach velocities in Fig. 9b. Stem S1ST with the lowest flexural rigidity experiences the least drag force per length while S2ST with the highest flexural rigidity experiences the highest drag force per length. The drag force values of the other two stems fall in between. Hence, the effects of flexural rigidity and stem morphology on the drag force are evident (Fig. 9b).

The calculated values of the drag coefficient for stems are plotted in Fig. 10a as a function of the Reynolds
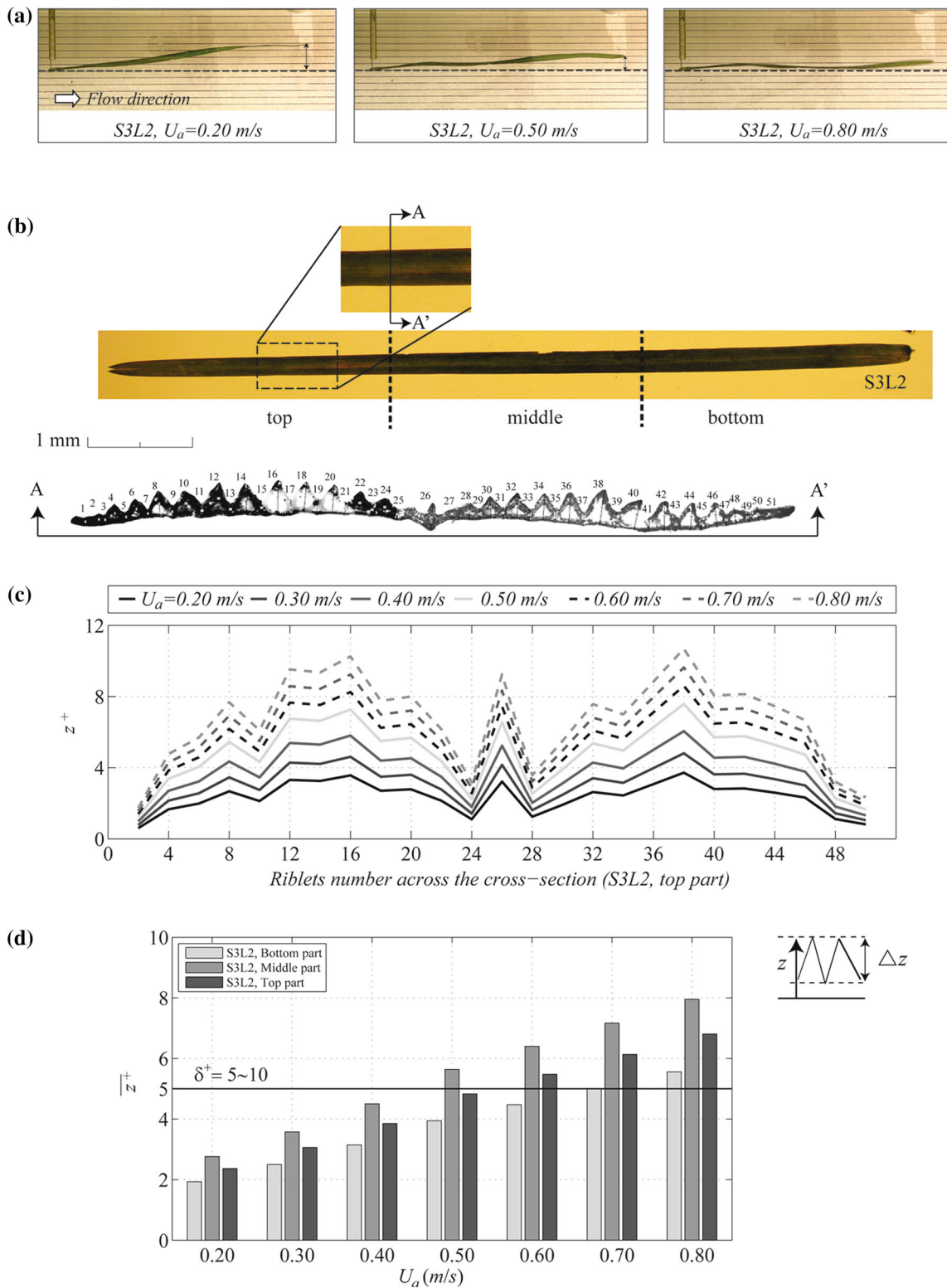
Fig. 8 Video images captured from the drag force and velocity experiments with the leaf S3L2 at $U_a = 0.2$, 0.50 and 0.80 m/s (**a**); leaf surface and the cross-section photos (**b**); the roughness heights of the upper leaf surface z^+ (**c**); and the average roughness heights over the leaf width of the leaf bottom, middle and top parts $\overline{z^+}$ versus the approach velocities (**d**)
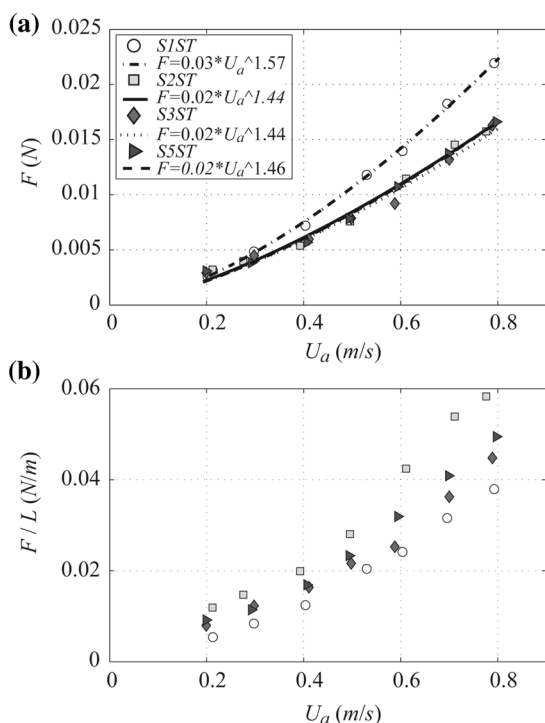
(a)

(b)

Fig. 9 The stem drag force F (**a**) and the drag force normalized by stem length, F/L (**b**) versus the mean approach velocity U_a

number Re_L. The data collapse around a declining power–type curve $C_d \propto Re_L^{-0.80}$, reflecting sharp decrease of C_d at smaller Re_L. This result, in combination with the Vogel numbers for stems, indicates that there is a possible drag control mechanism specific to the stems. On the other hand, the curves $C_d = f(Re_L)$ for stems are much higher than those for leaves as one could expect due to the differences in morphologies and flexural rigidities. The standard deviations σ_d follow a trend of linear increase with Re_L for all stems (Fig. 10b), with the highest values for S2ST and lowest for S1ST. However, the $CV(Re_L)$ values for all stems except S1ST are similar and become constant at highest Re_L (Fig. 10c). The plots of skewness of the drag force (Fig. 10d) do not reveal any significant differences between the stems, showing that the S_d values randomly fluctuate around 0. Hence, the probability distribution of the drag force for stems is expected to be symmetric around the mean. The plots of kurtosis K_d are also similar for all stems demonstrating a tendency to decrease from approximately 0.20 at lowest Re_L to -0.20 at highest Re_L, with change of the K_d sign occurring at approximately $Re_L = 1.5 \times 10^5$ (Fig. 10e).

Turbulence effects on drag force bulk statistics

The plots of the drag standard deviation σ_d versus the approach velocity standard deviation σ_{u_a} resemble an

expected trend $\sigma_d \propto \sigma_{u_a}^2$ (Fig. 11a), similar to the leaf–flow interactions in Fig. 5a. However, the ratio σ_d/σ_{u_a} reveal nearly linear relations with Re_L predicted by $\sigma_d/\sigma_{u_a} \propto U \propto Re_L$ (Fig. 11b), in contrast to leaves where the curves $\sigma_d/\sigma_{u_a} = f(Re_L)$ exhibit a concave form. The data separation in Fig. 11b is likely due to variability of the product $(A_w C_d)$ among the stems. Similar to leaves, stems suppress upstream turbulence, but at a lesser degree (compare Figs. 5c with 11c).

Spectral analysis of the drag force and flow velocity

A spectral analysis, similar to the leaves (Fig. 6), is shown in Fig. 12 using stem S2ST as a typical example. The spectra of the approach velocities are statistically indistinguishable from those for leaf S2L4 in Fig. 6, as the ADV was placed far away from the DMD and hence no effect of either leaf or stem is seen in the approach velocity spectra. The effect of the stem S2ST on the downstream velocity spectra is similar to that of a leaf (Fig. 6b), i.e., the low-frequency spectral components are suppressed up to 30–60 %, with little or no suppression effect at a high-frequency range (Fig. 12c). The spectra of the drag force for stem S2S4 bear a resemblance to those from the leaf experiments but with a stronger noise floor (Fig. 12d). The stem force transfer function (SFTF) shown in Fig. 12e reveals two well-developed 'hills' (approximately within the same frequency ranges as for leaves, reflecting effects of large-scale turbulence and stem-length scale instabilities), with a signature of an additional third peak at the highest frequencies. This third peak in SFTF has not been properly resolved and could relate to instabilities at a stem diameter scale.

Cross-correlations

With increase in U_a, the maximum correlation levels in $R_{u_a\hat{F}_m}$ and $R_{\hat{F}_m u_d}$ also increase while the prevailing time scales of these cross-correlation functions decrease (Fig. 13a, b). The latter suggests that the spatial scales ($\sim U_a$ times time scales) are approximately independent of the mean approach velocity being comparable to the flow depth. This result complements the findings from the spectral analysis and indicates that the main contributions to the fluctuating drag force come from the fluctuating approach velocity due to the large-scale turbulence. The maximums of the cross-correlation functions $R_{u_a u_d}$ between the approach and downstream velocities are almost the same for all mean approach velocities, being less than those for $R_{u_a\hat{F}_m}$ and $R_{\hat{F}_m u_d}$ (Fig. 13c). The maxima of $R_{u_a\hat{F}_m}$, $R_{\hat{F}_m u_d}$, and $R_{u_a u_d}$, averaged over all stems, versus the mean approach velocities are shown in Fig. 13d, which highlights that $R_{u_a\hat{F}_m}$ is most sensitive to changes in U_a.
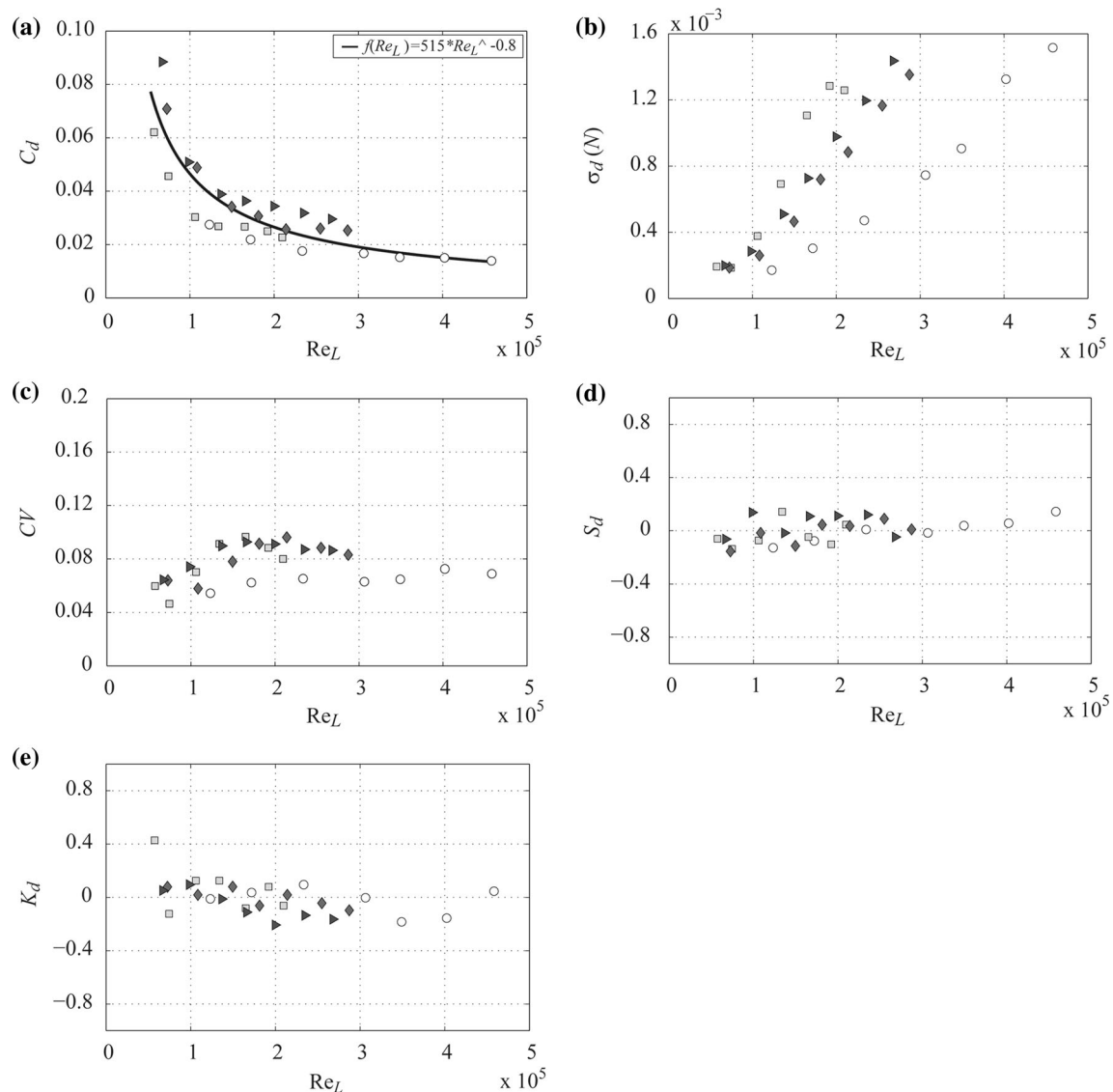
Fig. 10 The stem drag coefficient C_d (**a**); drag standard deviation σ_d (**b**); coefficient of variation CV (**c**); skewness coefficient S_d (**d**); and kurtosis coefficient K_d (**e**) versus the Reynolds number Re_L; symbols are the same as in Fig. 9

Possible drag control mechanisms

Although the stems have cylindrical cross-sections and much higher flexural rigidities, compared to leaves, the data suggest that they can also reduce the drag force under high flow velocities. Indeed, the stem Vogel numbers were found to be less than zero, ranging between -0.43 and -0.56. The captured images from the experiments with the stems demonstrate that the stems reconfigure under high flow velocities (Fig. 14) which explains negative Vogel numbers. At low U_a, the bending of the stem is small but with velocity increase the stem significantly bends (Figs. 14b, c) resulting in a reduced form drag. However, we did not observe any stem undulation similar to the leaf dynamic reconfiguration. Instead, there were stem

oscillations/vibrations due to flow separation and vortex shedding from its cylindrical body.

Shoot experiments

Bulk statistics of drag force

The mean drag force as a function of the mean approach velocity is shown in Fig. 15a for seven shoots differing in length, wetted area and number of leaves. These differences are reflected in the separation of individual curves $F = f(U_a)$, with the highest magnitudes of F observed for the largest, in terms of the wetted area, shoot S3WS. Similar to the experiments with leaves and stems, the mean drag forces acting on shoots are strongly correlated with
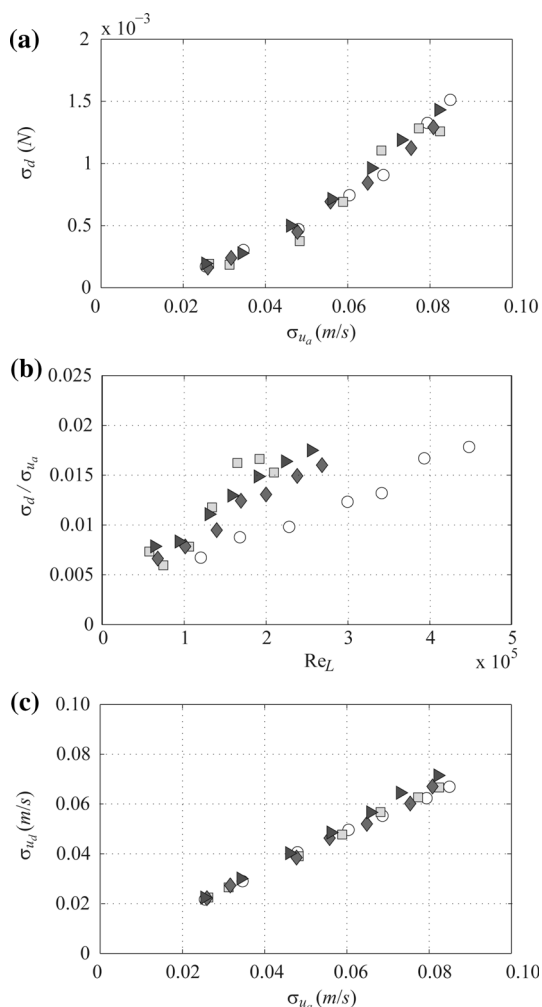
Fig. 11 The drag force standard deviation σ_d versus the standard deviation of the approach velocity σ_{u_a} (**a**); the ratio of σ_d to σ_{u_a} versus Re_L (**b**); and the standard deviation of the downstream velocity σ_{u_d} versus the standard deviation of the approach velocity σ_{u_a} (**c**) for all stems; symbols are the same as in Fig. 9

the approach velocities, exhibiting negative Vogel numbers (i.e., $\alpha = -0.43$ to -0.63). Consequently, the shoot drag coefficients C_d, vary between 0.035 and 0.01, appreciably decrease with increasing U_a and, thus, Re_L (Fig. 15b). This behaviour is likely due to plant reconfiguration such as bending, streamlining, and folding. The data on the standard deviation $\sigma_d = f(\mathrm{Re}_L)$ follow a similar tendency as in the drag force plots (Fig. 15c). At low Re_L, the σ_d increases slowly and does not differ much between shoots while at higher Re_L the curves $\sigma_d = f(\mathrm{Re}_L)$ become steeper and diverge. The highest σ_d at large Re_L is observed for the largest shoot S3WS, while shoot S5WS exhibits the least drag force variability. This curve stratification reflects differences in the product $(A_w C_d)$ among shoots. The coefficient of variation $CV = f(\mathrm{Re}_L)$ is almost constant in the studied range of Re_L (Fig. 15d). It randomly fluctuates

around 0.06, which is considerably smaller than CV for stems and leaves. No significant differences among shoots can be seen in the plots of skewness S_d and kurtosis K_d coefficients (Fig. 15e, f), which deviate from Gaussian values only slightly ($S_d \sim 0.04$ and $K_d \sim -0.09$).

Effect of shoot components superposition on the total drag force

In order to determine the potential superposition effects of the shoot components on the total drag force, we computed the ratios of the total shoot drag force to the sum of the drag forces experienced by the individual shoot components measured separately (Fig. 16). Shoots S1 and S2 feel up to 25 % lower overall drag compared to the sums of the drag forces acting on their individual components in isolation. The other two shoots, S3 and S5, experience much weaker drag reduction (if any). From Table 2 we can see that the lengths and wetted areas of shoots S1 and S2 are similar (i.e., $L_{S1WS} = 0.65$ m, $L_{S2WS} = 0.61$ m and $A_{wS1WS} = 0.0137$ m^2, $A_{wS2WS} = 0.0132$ m^2) being much smaller than those of shoots S3 and S5 (i.e. $L_{S3WS} = 0.79$ m, $L_{S5WS} = 0.81$ m and $A_{wS3WS} = 0.0209$ m^2, $A_{wS5WS} = 0.0153$ m^2). Hence, shoot length, wetted area, positions of the leaves around the stem (i.e., shoot morphology), and the leaf and stem biomechanics should influence the way of how the superposition of shoot components is reflected in the overall drag. It is plausible that younger (smaller) shoots are more flexible and thus more efficient in drag control than older (longer) shoots.

Turbulence effects on drag force bulk statistics

The dependence of the drag bulk statistics for shoots on the approach velocity is similar to that for leaves and stems. The standard deviation of the drag force σ_d can be approximated well as $\sigma_d \propto \sigma_{u_a}^2$ (Fig. 17a) while the ratio $\sigma_d / \sigma_{u_a} \propto U \propto \mathrm{Re}_L$ (Fig. 17b), in agreement with an approximate relationship $\sigma_d \approx 0.5 \rho A_w C_d \sigma_{u_a}^2$. The data points for all shoots closely collapse together with an exception of the largest shoot S3WS (likely the effect of the largest product $A_w C_d$). The level of suppression of the velocity variations behind shoots is similar to that for leaves and stems (Fig. 17c).

Spectral analysis of drag force and flow velocity

The approach and downstream velocity spectra and the shoot velocity transfer function resemble the results for leaves and stems (Fig. 18a–c). However, one may also note that the suppression of the low-frequency spectral components is stronger in the case of shoots (Fig. 18c), due to their more complex structure. The drag force spectra for
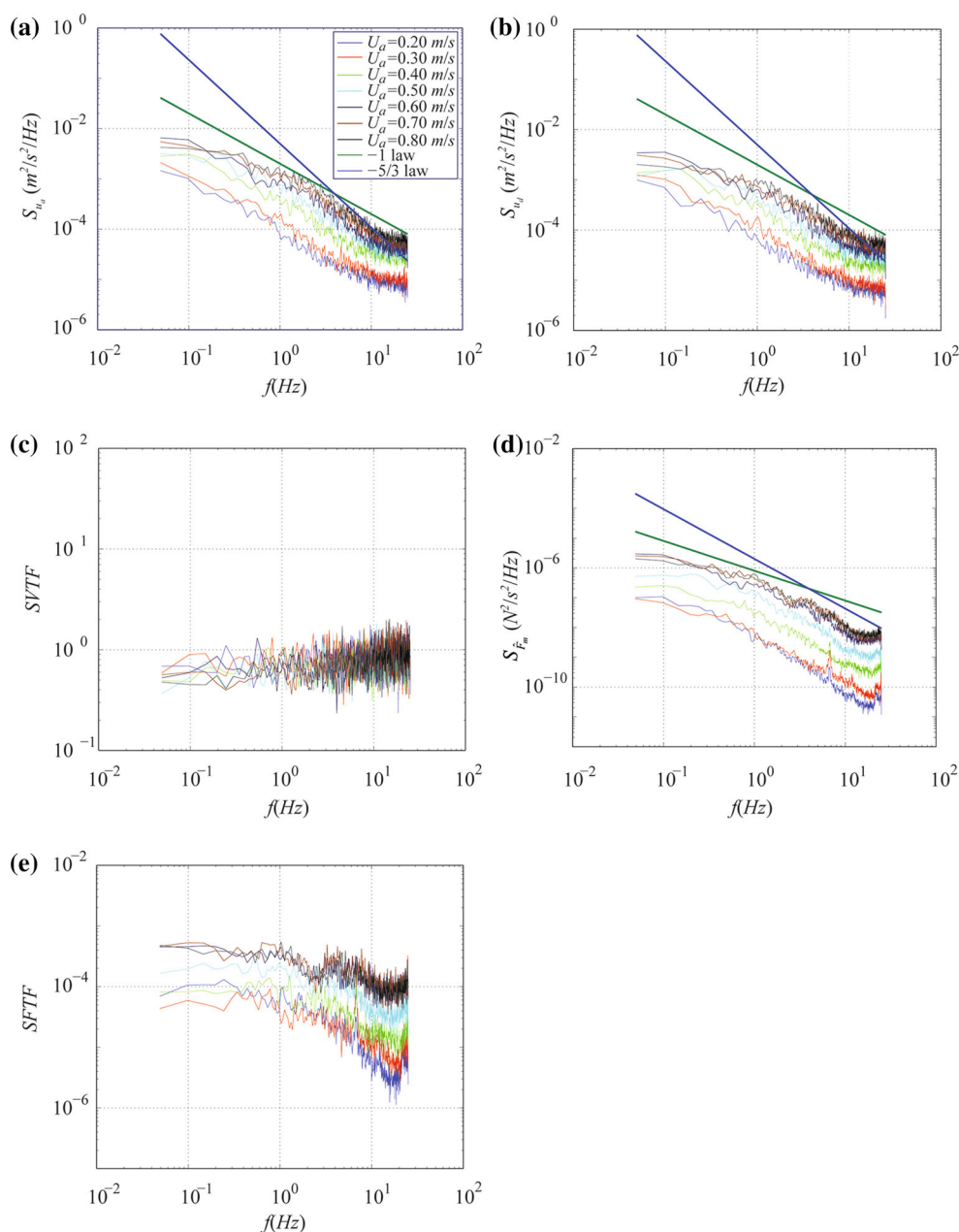
Fig. 12 Power spectra of approach (**a**) and downstream (**b**) velocities, and drag forces (**d**), stem velocity transfer (**c**) and stem force transfer (**e**) functions for stem S2ST

shoots are similar in shape to those for stems and leaves as well (Fig. 18d), although with some distinct 'hills' at 3.5 and 20 Hz, especially profound at high approach velocities (as it was already mentioned, the peak at 7 Hz reflects flume micro-vibration). These features are reflected in the force transfer function (Fig. 18e) and likely emerge as a result of active (self-induced) interactions between flow and shoots, in addition to the passive interactions in response to large-scale turbulence. Another distinct feature of the SHFTF is a sharp reduction of the spectral energy at $f > 20$ Hz, which is probably due to the 'self-cancelling'

superposition of incoherent small-scale fluctuations of different leaves and the stem.

Cross-correlations

The cross-correlation functions $R_{u_a \hat{F}_m}$, $R_{\hat{F}_m u_d}$ and $R_{u_a u_d}$ for the shoots are shown in Fig. 19. If the shoot $R_{u_a \hat{F}_m}$ closely resembles the cross-correlations for stems and leaves, the curves $R_{\hat{F}_m u_d}$ and $R_{u_a u_d}$ appear to be quite different, both having much lower correlations. This later finding highlights the significant effect of shoots on the wake

Fig. 13 Cross-correlation functions between approach velocity and drag force $R_{u_a \hat{F}_m}$ (**a**); between drag force and downstream velocity $R_{\hat{F}_m u_d}$ (**b**); and between approach velocity and downstream velocity $R_{u_a u_d}$ (**c**) for stem S2ST; and the maximum cross-correlation coefficients $MR_{u_a \hat{F}_m}$, $MR_{\hat{F}_m u_d}$ and $MR_{u_a u_d}$ averaged over all stems (**d**)
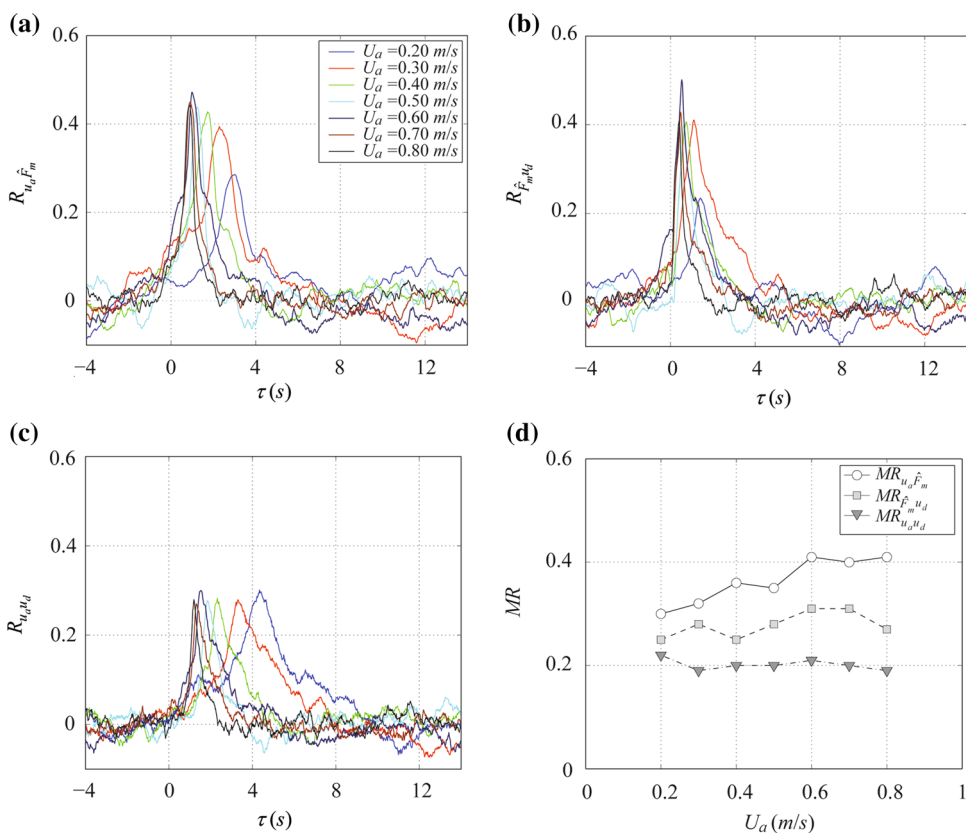
turbulence that is largely de-correlated by the shoots from the approach large-scale turbulence (in qualitative agreement with the spectral analysis above). The maximum cross-correlations $R_{u_a \hat{F}_m}$, $R_{\hat{F}_m u_d}$ and $R_{u_a u_d}$ averaged over all seven shoots are shown in Fig. 19d versus the mean approach velocities. The maximum of $R_{u_a \hat{F}_m}$ increases with increasing velocity while the maxima of $R_{\hat{F}_m u_d}$ and $R_{u_a u_d}$ vary only slightly, similarly to leaves and stems.

Possible drag control mechanisms

The data shown above suggest that at high flow velocities plant shoots may effectively reduce drag forces imposed by flow. To illustrate potential drag-reduction mechanisms, here we examine video images for shoot S3SW recorded at $U_a = 0.20$, 0.50 and 0.80 m/s (Fig. 20). The visual observations and image analysis suggest two possible drag control mechanisms of plant shoots. The first mechanism relates to the form drag reduction. With increasing velocity, the shoot bends and reorients itself in the flow direction, thus reducing the frontal area and form drag. In addition to this passive reconfiguration, the individual leaves around the stem exhibit a dynamic reconfiguration; i.e., they undulate, likely leading to further reduction of the total form drag. The second mechanism relates to skin friction (or viscous drag reduction). The leaves coalesce

around the stem, thereby reducing the exposed surface area and the porosity of the shoot, and hence flow passes around the shoot rather than through it. This mechanism reduces the effective wetted area and therefore the total viscous drag. The efficiency and possible dominance of these two mechanisms depend on shoot morphology (e.g., positions of the leaves around the stem) and plant tissue biomechanics.

Discussion

The results reported in this paper set the scene for both ecological and physical interpretations. Some of them will be briefly discussed here while others, we hope, will emerge in follow-up studies of flow–plant interactions.

At the leaf scale, we found that due to leaf flexibility the drag force depends on the approach velocity non-linearly, as $F \propto U^{2+\alpha}$, with the drag coefficient decreasing with increase in velocity. The Vogel numbers α varied from -0.25 to -0.70, decreasing with the leaf flexural rigidity, despite a few outliers, and on average being equal to -0.50. Our estimates of α cover the same range as reported for tree leaves in Vogel (1989), in spite of tree leaves being morphologically and structurally very different from the leaves of *G. fluitans*. Interestingly, our results for
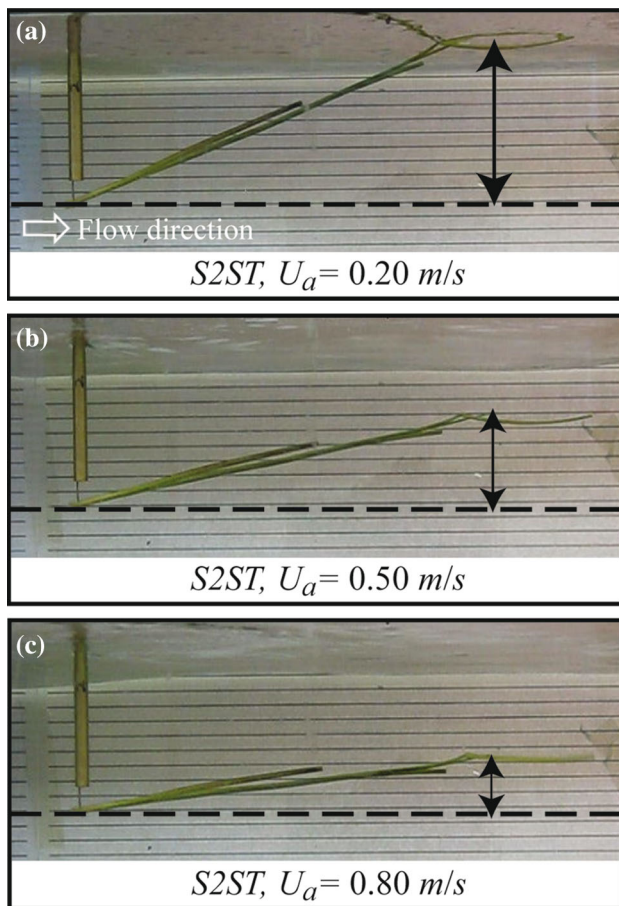
Fig. 14 Examples of video images captured in experiments with the stem S2ST at $U_a = 0.2$, 0.50 and 0.80 m/s

G. fluitans appeared to be also consistent with the data reported in Albayrak et al. (2012) for their modeled rectangular (strip-like) artificial leaves that had flexural rigidities close to that of *G. fluitans*. This similarity is encouraging as it highlights possibilities for physical modeling of plants with appropriately selected materials.

It is also useful to compare our data with phenomenological, experimental, and numerical studies of rectangular plastic plates and thin fibers (Alben et al. 2002, 2004; Zhu 2008), where the Vogel number α was found to be close or equal to $-2/3$. Alben et al. (2002) studied the flow-fiber interactions in a thin 2D soap flow and identified a dimensionless control parameter η as a ratio of fluid kinetic energy to elastic potential energy. This parameter governs the underlying mechanical interaction between flow and the flexible fiber. They observed two different interaction regimes between flow and fiber depending on η. For $\eta \ll 1$, the fiber bends only slightly and the drag force scales with the squared flow velocity, as for a rigid body at a high Reynolds number. For $\eta \gg 1$, the fiber significantly bends; i.e. pressure forces dominate over the elastic bending forces and consequently the drag on the fiber scales with $U_a^{4/3}$

(hence $\alpha = -2/3$). Similar results were reported by Zhu (2008) based on a numerical study at large plate Reynolds numbers. Although we did not parameterize leaf reconfiguration mechanisms with η in this investigation, the image analysis of leaf motions and our visual observations revealed leaf reconfiguration mechanisms similar to those observed for the flexible flat plates and fibers. At low velocities, leaves bended only slightly and thus pressure drag dominated the total drag. At higher velocities, the leaves bended strongly and aligned with the flow leading to a significantly reduced pressure drag. In addition to this static reconfiguration, in order to lessen the dynamic load at high velocities, leaves undulated in the flow direction. This form of reconfiguration (that can be defined as a dynamic reconfiguration) is not accounted in fiber and plate studies and could contribute to the observed variability of the Vogel number in our experiments and its deviation from $\alpha = -2/3$. Another potentially significant drag reduction mechanism worth mentioning here relates to the skin (viscous) friction that can be suppressed by surface riblets (Fig. 8) up to 10 % (e.g., Walsh and Lindemann 1984; Tani 1988). This mechanism and its role in flow–leaf interactions deserve a more detailed study.

Levin et al. (1997) experimentally investigated the drag characteristics of streamers (i.e. slender rectangular flags, ribbons, streamers, strips) made of eight different materials with aspect ratios L/B ranging from 2 to 22 and at wind velocities up to 25 m/s. Similarly, Carruthers and Filippone (Carruthers and Filippone 2005) studied the effect of aspect ratio on the drag for streamers made of cotton fabric, nylon, and polyester with $L/B = 3.3$, 10, 20 and 30. Both studies show that the drag coefficient decreases with increasing aspect ratio of the streamer (all other parameters being the same). However, in the present study an opposite trend is observed up to $L/B = 70$ while beyond this point, the trend is similar. This can be attributed to differences: (I) in the range of aspect ratio and (II) in material properties such as roughness, flexural rigidity, weights and homogeneity between the above cited studies and the tested leaves in this study. Especially, the difference between leaf biomechanical properties possibly causes this opposite trend at low aspect ratios while this effect diminishes at high aspect ratios. A further investigation is required to clarify this issue.

The cross-correlation analysis of the drag force, approach velocity, and downstream velocity revealed that the drag force was most highly correlated with the approach velocity. This strong correlation suggests a close linear coupling between the large-scale turbulence of the approach flow and leaf response. In other words, the drag force fluctuations may be viewed, to a certain degree, as a passive reflection of the fluctuating approach velocity [in agreement with $F(t) \propto C_d(t)A(t)u^2(t)$]. In addition to this
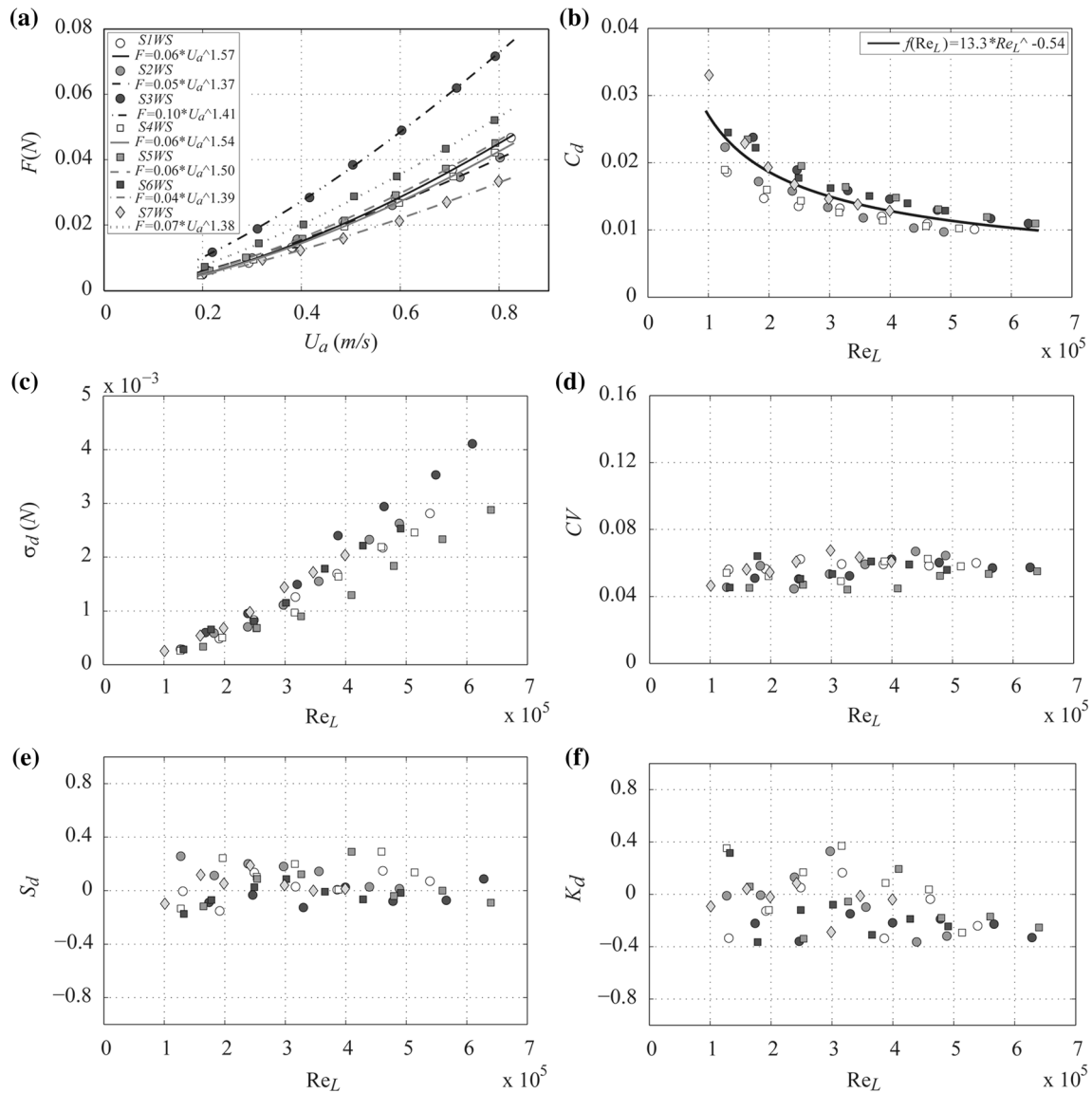
Fig. 15 The shoot drag force F versus the mean approach velocity U_a (**a**); shoot drag coefficient C_d (**b**), drag standard deviation σ_d (**c**), coefficient of variation CV (**d**), skewness S_d (**e**), and kurtosis K_d (**f**) versus the Reynolds number Re_L

passive linear interaction, the concave form of $\sigma_d/\sigma_{u_a} = f(Re_L)$ in Fig. 5b highlights one more, nonlinear, mechanism that likely relates to the leaf instability that suppresses the effects of upstream turbulence. The power spectral densities and transfer function of the leaf drag force and approach velocity support this conjecture and indicate the spatial scales responsible for the linear passive interactions ($\sim$3–5 flow depths—scale of large eddies) and non-linear active interactions ($\sim$0.3–0.5 leaf lengths—scale of leaf instabilities, consistent with Siniscalchi and Nikora 2013). A further investigation of the relationships between the turbulent upstream flow and leaves is required to identify the effects of scale separation (i.e., ratio of the turbulence scale to the leaf scale) and the nature of leaf instabilities.

Biophysical processes such as the uprooting of plants or breakage of plant leaves are likely determined by extremes values of the drag force, and thus the knowledge of drag force statistics is highly relevant for the understanding of plant ecology. In this regard it is interesting to recall Figs. 3 and 4 that show, in general, older and less flexible leaves experienced higher drag forces per leaf length and higher drag fluctuations (expressed in terms of the standard deviation) compared to younger more flexible leaves. This finding suggests that there may be a self-pruning mechanism that plants employ, using flexural rigidity, to get rid of older leaves by enhancing extreme drag forces acting on them.

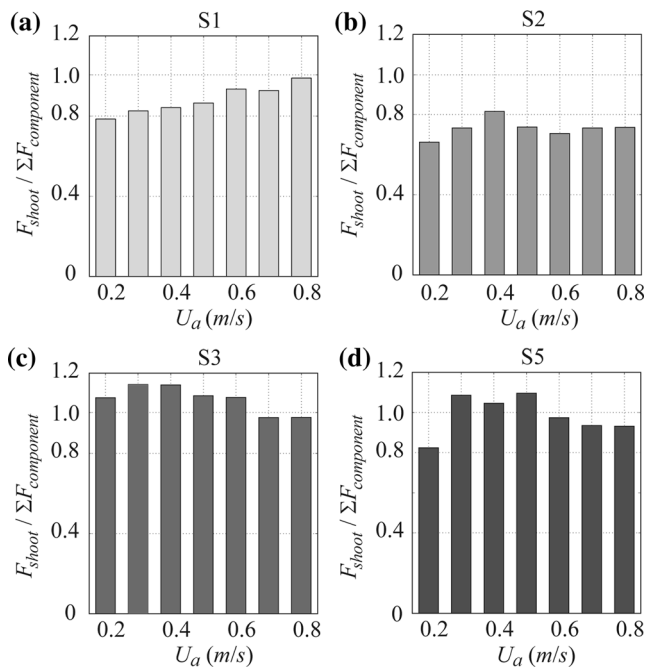The obtained data also allow us to draw some conclusions regarding the development of the leaf boundary

Fig. 16 The ratio of shoot drag forces to the sum of the drag forces of the shoot components (leaves + stem) for shoots S1, S2, S3 and S5 at seven different velocities

layer (LBL), although it was not measured directly in our study. The properties of LBLs are important for mass, momentum, gas, and heat exchanges between leaves and their environment, which occur across LBLs. A useful discussion of terrestrial LBLs is given in Schuepp (1993) while information on the aquatic or semi-aquatic LBLs is limited to their biochemical properties (Jones et al. 2000; Madsen and Maberly 2003). For a smooth flat plate, the critical Reynolds number for transition from a laminar boundary layer to the turbulent boundary layer is $Re_{Lc} \approx 5 \times 10^5$ (Schlichting and Gersten 2000) while for flat rectangular leaf models Re_{Lc} was found to be 1×10^4 to 3×10^4. These values are valid for the case of laminar free stream (approach) flow (Chen et al. 1988; Schuepp 1993). For turbulent free stream flow, Re_{Lc} is expected to be less than 2×10^4. Considering that the flows in our study were fully turbulent (Table 1), we may safely conclude that the Re_L values (0.5×10^5 to 4×10^5) were higher than critical. However, Fig. 4a highlights that the leaves' C_d were much higher than those for both laminar and turbulent LBLs. Several factors could contribute to this difference. First, the total drag (and thus C_d) has been highly influenced by the leaf inclination in the flow that was especially profound at low approach velocities. With increase in flow velocity, the leaf alignment along the flow improved and as a result the drag coefficient sharply reduced, still being appreciably higher than that for the turbulent LBL. This remaining difference could be due to
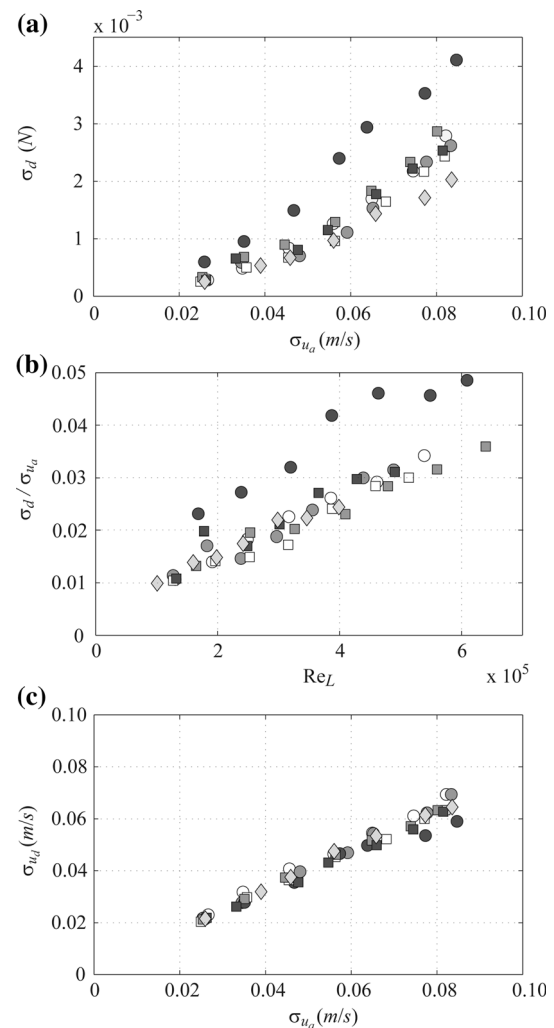

Fig. 17 The drag force standard deviation σ_d versus the standard deviation of the approach velocity σ_{u_a} (a); the ratio of σ_d to σ_{u_a} versus Re_L (b); and the standard deviation of downstream velocity σ_{u_d} versus the standard deviation of the approach velocity σ_{u_a} (c) for all shoots

the leaf surface roughness and leaf fluttering, which effects are not fully clear and need deeper exploration. Although the noted features of LBLs have been mainly discussed in terms of the drag force, they are as important for substance transfer and uptake by the leaves. The key parameter controlling such transfers is the thickness of the LBL that could be easily determined if the leaves obeyed the conditions of conventional laminar or turbulent boundary layers. The deviations from these conditions make such estimates highly uncertain and highlight another task for the forthcoming studies of leaf–flow interactions.

Stems represent another important plant element. Their spatial scale is similar to that of leaves but their role in plant functioning is different and hence they have distinctly different morphology and biomechanics. As a result, the stem drag coefficients C_d were found to be

Fig. 18 Power spectra of approach (**a**) and downstream (**b**) velocities, and drag forces (**d**), shoot velocity transfer (**c**) and shoot force transfer (**e**) functions for shoot S2WS
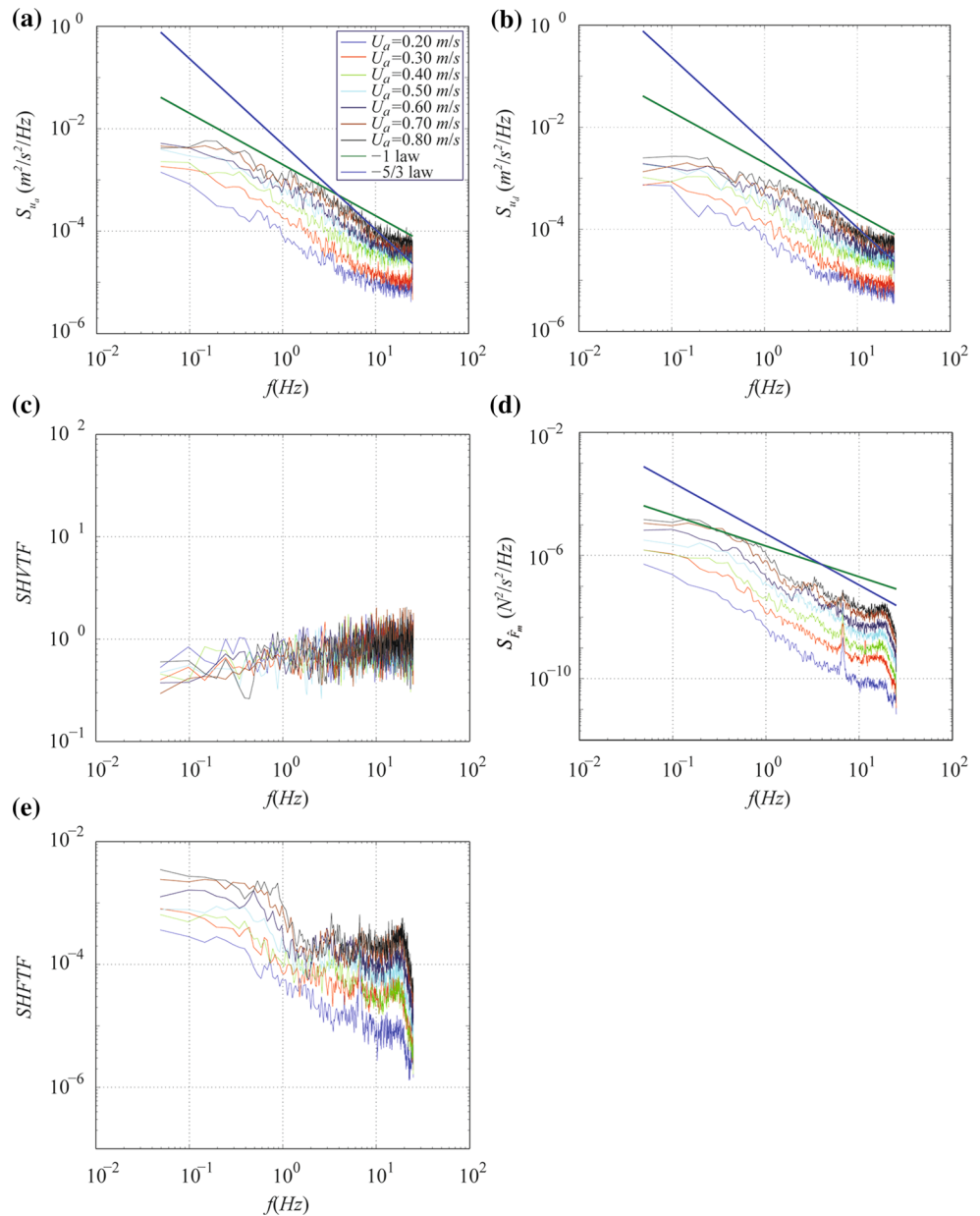
almost two times higher than those for leaves within the same range of Re_L. On the other hand, the average Vogel number for stems was similar to that of leaves, i.e., $\alpha = -0.50$, indicating, together with the image analysis (Fig. 14), that stems also were capable of reconfiguration in order to control the drag acting on them. In contrast to leaves, however, stems bended at their bottom ends glued to the DMD, with no profound bending or deformation along the stems (Fig. 14). It is worth comparing our findings with Gosselin and de Langre (2011) who studied both rigid filaments and flexible filaments with a flexural rigidity similar to that of the present stems. They mainly focused on static reconfiguration and neglected dynamic effects of upstream turbulence and vortex shedding.

Gosselin and de Langre (2011) found that due to static reconfiguration, the drag–velocity relation for flexible filaments was not quadratic while it was quadratic for rigid filaments. Our findings for natural stems are in agreement with this result. As far as dynamics of flow–stem interactions are concerned, we found that similar to leaves, there are at least two distinct interaction modes (Fig. 12): a passive mode at a scale of large eddies (several flow depths) and an active mode at a stem scale. However, the effect of the stem-scale active interactions is different from that for leaves. The relation $\sigma_d/\sigma_{u_a} = f(Re_L) \propto U \propto Re_L$ was found to be quasi-linear as it would be for the passive interactions when the drag variation is simply a reflection of $F(t) \propto C_d(t)A(t)u^2(t)$
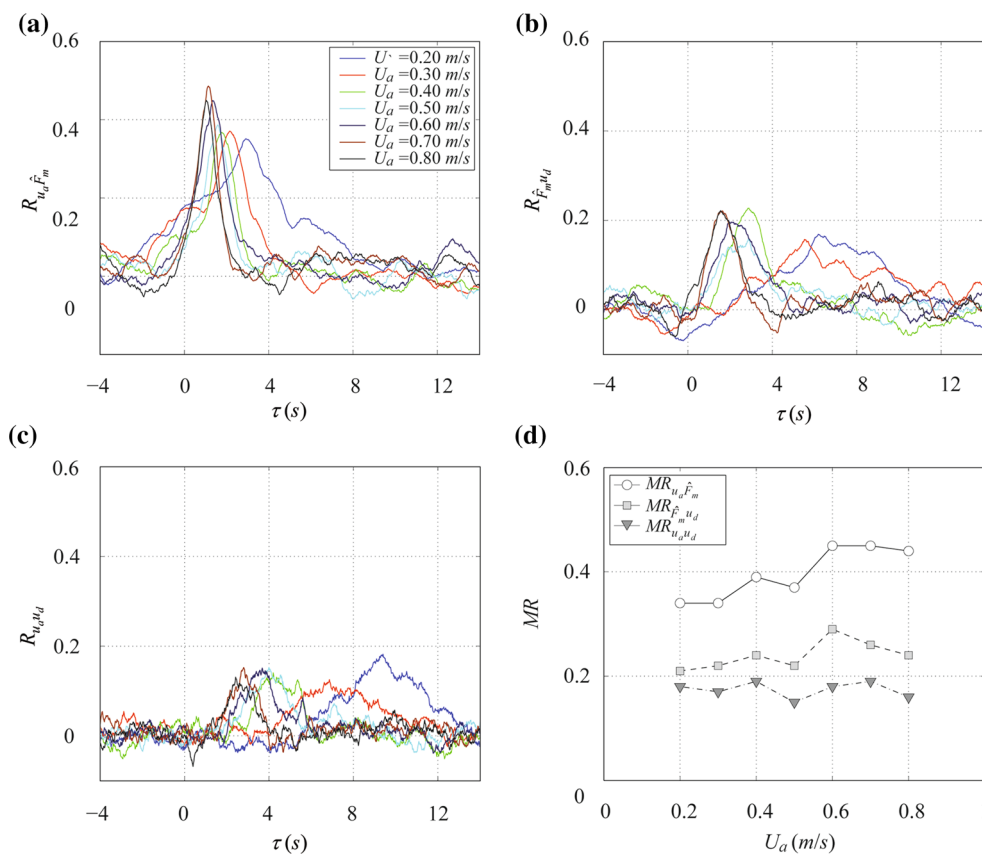
Fig. 19 Cross-correlation functions between approach velocity and drag force $R_{u_a \hat{F}_m}$ (**a**); between drag force and downstream velocity $R_{\hat{F}_m u_d}$ (**b**); and between approach velocity and downstream velocity $R_{u_a u_d}$ (**c**) for shoot S2WS; and the maximum cross-correlation coefficients $MR_{u_a \hat{F}_m}$, $MR_{\hat{F}_m u_d}$ and $MR_{u_a u_d}$ averaged over all shoots (**d**)
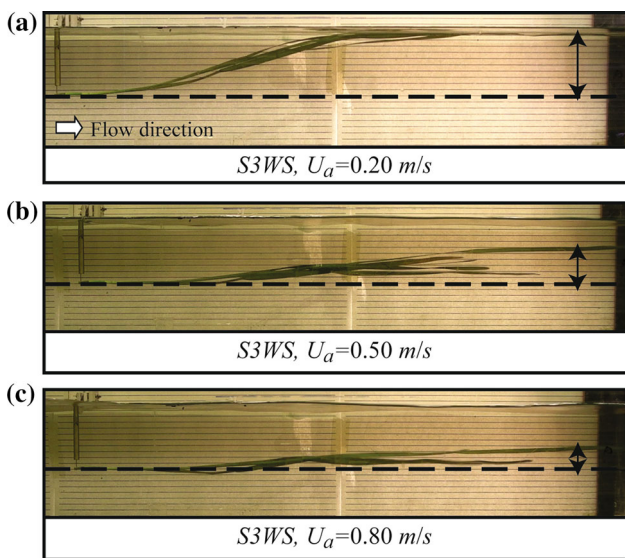

Fig. 20 Examples of video images captured in experiments with shoot S3WS at $U_a = 0.2$, 0.50 and 0.80 m/s

(leading to $\sigma_d \approx 0.5 \rho A_w C_d \sigma_{u_a}^2$ and $\sigma_d / \sigma_{u_a} \propto Re_L$). In other words, the effects of active interactions at a stem scale were not as visible in the overall drag variability as

in the case of leaves. This behavioural difference from leaves is likely because stems were oscillating as solid bodies, without showing undulations typical for leaves. This may explain why the range of the Vogel number for stems was narrower (-0.43 to -0.56) than for leaves (-0.25 to -0.70). In addition to the above interaction modes, it is worth mentioning that the drag spectra and stem transfer functions (Fig. 12) also suggest a third interaction mode at high frequencies, which is likely generated by flow separations and vortex-shedding from stems. This third interaction mode, however, was not properly resolved in our measurements. The information on flow–stem interactions reported in this paper may be helpful for better understanding of plant ecology, particularly related to plant uprooting and breakage. Indeed, the breakage of a single stem may often lead to the complete plant detachment from the bed making stems critically important for whole plant performance.

The combined effects of leaves and stems have been evaluated using whole shoots. They responded to flow loads by stem bending (i.e., by aligning with the flow) and by leaves streamlining and coalescing around the stem (Fig. 20). This complex reconfiguration resulted in the

shoot Vogel number in the range from −0.63 to −0.43, with $\alpha = -0.55$ on average. Figure 16 suggests that, altogether, leaves and stems at a shoot scale may exhibit additional drag reduction, compared to simple sum of leaves and stems considered in isolation. Furthermore, our data support a conjecture that younger (smaller) shoots are more efficient in drag reduction compared to older (larger) shoots. Thus, our 'self-pruning' hypothesis proposed above for leaves can be expanded to also cover the shoot scale.

The drag force spectra and shoot transfer functions appeared to be similar, not surprisingly, to those for leaves and stems. They also reveal several ranges of scales that likely reflect effects of large-scale turbulence and shoot-scale instabilities. The latter may be a result of either coherent behaviour of most leaves within the shoot or interactions which are specific to the shoot scale only. This issue is not yet clear and needs further exploration. In contrast to stems and leaves, there is a clear suppression of drag fluctuations at high-frequencies which is most likely due to the 'self-cancelling' superposition of incoherent small-scale fluctuations of different leaves and the stem. This 'self-cancelling' effect may explain the reduced coefficient of drag variation, compared to leaves and stems.

The plant-flow interactions at leaf, stem and shoot scales described above should be also discussed with respect to potential adaptations of *G. fluitans* to hydraulic habitats. We observed the leaves of *G. fluitans* shoots to float at or close to the surface at low flow velocities (0.2 m/s), but to streamline along the shoot at higher velocities also becoming fully submerged (Fig. 20). *G. fluitans* has been mainly reported to inhabit slow-flowing streams and river margins as well as flooded meadows and lakes (Preston and Croft 2001; Miler et al. 2012). This is reflected in its biomechanical properties that characterize it as a bending plant with a high flexural rigidity, high breaking force and high breaking stress (Miler et al. 2012). Leaves are typically floating on the water surface which might be an adaptation to increase the exposure of photosynthetically active tissues towards sunlight. At flow velocities higher than 0.2 m/s (Fig. 20), leaves might become submerged and streamline with the stem at short periods of high water discharge in typically slow-flowing rivers, e.g. during temporary periods of high rainfall and snowmelt. Hence, *G. fluitans* might survive short periods of high velocities during spates but needs slow flow velocities below 0.5 m/s to persist, grow and develop larger plant patches. Furthermore, as a semi-aquatic grass *G. fluitans* also needs to develop a second type of emerged, upright growing terrestrial shoots for reproduction (Preston and Croft 2001; Miler et al. 2012). This is only possible in slow-flow environments.

Conclusions

Our paper reports, for the first time, a systematic study of statistical characteristics of plant–flow interactions at leaf, stem, and shoot scales using *G. fluitans* as an example. The analyzed statistics include mean values, standard deviations, skewness, kurtosis, power spectra, transfer functions and cross-correlation functions of the approach flow velocity, drag force acting on the plant elements, and wake flow velocity. Altogether these parameters provide a quite comprehensive characterization of plant hydraulic performance that should underpin the follow-up studies of biophysics and ecology of aquatic plants.

The key findings of this work include:

1. Visual observations, image analysis and drag–velocity relations revealed multiple scale-specific mechanisms of static and dynamic reconfiguration that plants employ for the effective drag control. The Vogel number, which is a quantitative measure of the total reconfiguration, varied around ~ -0.5 for all plant elements, although the exact mechanisms underpinning this value are likely to be element specific.
2. Bulk drag force statistics and drag coefficients exhibit similar general behavior for all studied elements. The noted specific differences between the elements relate to the differences in their morphology and flexural rigidity.
3. The plant element–flow interactions can be subdivided into two classes: (1) passive interactions when the drag variability is due to the temporal variability of the wetted and frontal areas and squared approach velocity (due to the large-scale turbulence); and (2) active interactions representing a range of element-specific instabilities that depend on the element flexural rigidity and morphology.
4. The findings of plant–flow interactions at leaf, stem and shoot scales suggest that *G. fluitans* has successfully adapted, in terms of drag forces, to its typical hydraulic habitat.

References

Albayrak I, Nikora V, Miler O, O'Hare M (2012) Flow–plant interaction at a leaf scale: effects of leaf shape, edge, roughness and flexural rigidity. Aquat Sci 74(2):267–286

Alben S, Shelley M, Zhang J (2002) Drag reduction through self-similar bending of a flexible body. Nature 420:479–481

Alben S, Shelley M, Zhang J (2004) How flexibility induces streamlining in a two-dimensional flow. Phys Fluids 16:1694–1713

Armanini A, Righetti M, Grisenti P (2005) Direct measurement of vegetation resistance in prototype scale. J Hydraul Res 43: 481–487

Boller ML, Carrington E (2006) The hydrodynamic effects of shape and size change during reconfiguration of a flexible macroalga. J Exp Biol 209:1894–1903

Carruthers AC, Filippone (2005) Aerodynamic drag of streamers and flags. J Aircraft 42:976–982

Chen JM, Ibbetson A, Milford JR (1988) Boundary-layer resistances of artificial leaves in turbulent air: I. leaves inclined to the mean flow. Bound Lay Meteorol 45:371–390

Dodds W (2002) Freshwater ecology. Concepts and environmental applications. Academic Press, London

Elder JW (1960) The flow past a flat plate of finite width. J Fluid Mech 9:133–153. doi:10.1017/S0022112060000979

Ennos AR (1999) The aerodynamics and hydrodynamics of plants. J Exp Biol 202:3281–3284

Fathi-Moghadam M, Kouwen N (1997) Nonrigid, nonsubmerged, vegetative roughness on floodplains. J Hydraul Eng ASCE 123:51–57

Goring D, Nikora V (2002) De-spiking ADV data. J Hydraul Eng ASCE 128:117–126

Gosselin F, de Langre E (2011) Drag reduction by reconfiguration of a poroelastic system. J Fluid Struct 27(7):1111–1123

Gosselin F, de Langre E, Machado-Almeida B (2010) Drag reduction of flexible plates by reconfiguration. J Fluid Mech 650:319–341

Green JC (2005) Further comment on drag and reconfiguration of macrophytes. Freshwater Biol 50:2162–2166

Järvelä J (2002) Flow resistance of flexible and stiff vegetation: a flume study with natural plants. J Hydrol 269(1/2):44–54

Jones JI, Eaton JW, Hardwick K (2000) The effect of changing environmental variables in the surrounding water on the physiology of Elodea nuttallii. Aquat Bot 66:115–129

Jumars PA, Eckaman JE, Koch E (2001) Macroscopic animals and plants in benthic flows. In: Boudreau BP, Jorgensen BB (eds) The benthic boundary layer. Oxford University Press, Oxford, pp 320–347

Koehl MAR (1999) Ecological biomechanics of bethic organisms: life history, mechanical design and temporal patterns of mechanical stress. J Exp Biol 202:3469–3476

Levin D, Daser G, Shpund Z (1997) On the aero dynamic Drag of Ribbons. AIAA 97–1525. pp 402–408

Luhar M, Nepf HM (2011) Flow-induced reconfiguration of buoyant and flexible aquatic vegetation. Limnol Oceanogr 56(6): 2003–2017

Madsen TV, Maberly SC (2003) High internal resistance to CO_2 uptake by submerged macrophytes that use HCO_3^-: measurements in air, nitrogen and helium. Photosyn Res 77:183–190

Miler O, Albayrak I, Nikora V, O'Hare M (2012) Biomechanical properties of aquatic plants and their effects on plant–flow interactions in streams and rivers. Aquat Sci 74(1):31–44

Nezu I, Nakagawa H (1993) Turbulence in open-channel flows. IAHR Monograph. A.A. Balkema, Rotterdam

Nikora V (2010) Hydrodynamics of aquatic ecosystems: an interface between ecology, biomechanics and environmental fluid mechanics. River Res Appl 26:367–384

Nikora V, Goring DG (2000) Flow turbulence over fixed and weakly mobile gravel beds. J Hydraul Eng ASCE 126:679–690

O'Hare MT, Hutchinson KA, Clarke RT (2007) The drag and reconfiguration experienced by five macrophytes from a lowland river. Aquat Bot 86:253–259

Oplatka M (1998) Stabilitat von Weidenverbauungen an Flussufern, Mitteilungen der Versuchsanstalt fur Wasserbau, Hydrologie und Glaziologie, No. 156, ETH Zurich (Doctoral Thesis)

Preston CD, Croft JM (2001) Aquatic plants in Britain and Ireland. Harley Books, Colchester, p 365, ISBN 0-946589-69-0

Sand-Jensen K (2003) Drag and reconfiguration of freshwater macrophytes. Freshwater Biol 48:271–283

Schlichting H, Gersten K (2000) Boundary layer theory. 8th revised and enlarged edition. Springer, Berlin

Schouveiler L, Boudaoud A (2006) The rolling up of sheets in a steady flow. J Fluid Mech 563:71–80

Schuepp PH (1993) Leaf boundary layers: Tansley review no. 59. New Phytol 125:477–507

Siniscalchi F, Nikora V (2013) Dynamic reconfiguration of aquatic plants and its interrelations with upstream turbulence and drag forces. J. Hydraulic Res 51(1):46–55

Statzner B, Lamouroux N, Nikora V, Sagnes P (2006) The debate about drag and reconfiguration of freshwater macrophytes: comparing results obtained by three recently discussed approaches. Freshwater Biol 51:2173–2183

Sukhodolov A (2005) Comment on drag and reconfiguration of macrophytes. Freshwater Biol 50:194–195

Tani I (1988) Drag reduction by riblet viewed as a roughness problem. Proc Jpn Acad B 64:21–24

Usherwood JR, Ennos AR, Ball DJ (1997) Mechanical adaptations in terrestrial and aquatic buttercups to their respective environments. J Exp Bot 48:1469–1475

Vogel S (1989) Drag and reconfiguration of broad leaves in high winds. J Exp Bot 40:941–948

Vogel S (1994) Life in moving Fluids, 2nd edn. Princeton University Press, Princeton

Vogel S (2009) Leaves in the lowest and highest winds: temperature, force and shape. New Phytol 183:13–26

Vollsinger S, Mitchell SJ, Byrne KE, Novak MD, Rudnicki M (2005) Wind tunnel measurements of crown streamlining and drag relationships for several hardwood species. Can J Forest Res 35:1238–1249

Walsh MJ, Lindemann AM (1984) Optimization and application of riblets for turbulent drag reduction. AIAA paper 84–0347, New York

Wilson CAME, Stoesser T, Bates PD, Batemann PA (2003) Open channel flow through different forms of submerged flexible vegetation. J Hydraul Eng ASCE 129:847–853

Xavier P, Wilson CAME, Aberle J, Rauch H P, Schoneboom T, Lammeranner W, Thomas H (2010) Drag force of flexible submerged trees." Proc. Hydralab Closing Event, 2–4 February 2010, Hanover, Germany

Zhu L (2008) Scaling laws for drag of a compliant body in an incompressible viscous flow. J Fluid Mech 607:387–400

Zhu L, Peskin C (2002) Simulation of a flapping flexible filament in a flowing soap film by the immersed boundary method. J Comput Phys 179:452–468

Zhu L, Peskin C (2007) Drag of a flexible fiber in a 2D moving viscous fluid. Comp Fluids 36:398–406